UNIVERSITY OF CALIFORNIA,
IRVINE

Mathematical modeling of tumor growth and angiogenesis

DISSERTATION

submitted in partial satisfaction of the requirements
for the degree of

DOCTOR OF PHILOSOPHY

in Mathematical, Computation and Systems Biology

by

Weihao Tang

Dissertation Committee:
Professor John S. Lowengrub, Chair
Professor Long Chen
Professor German A. Enciso

2024

TABLE OF CONTENTS

LIST OF FIGURES

Page

LIST OF TABLES

ACKNOWLEDGMENTS

> If you want the rainbow, you have to deal with the rain.
>
> *Augustus*

First and foremost, I would like to express my sincere gratitude to my supervisor, Prof. Dr. John S. Lowengrub, for his patience, guidance and support. John has consistently inspired and driven me to become an independent researcher and thinker. As an exceptional mentor, he has not only guided me in research, but he has also been an responsible leader who has taught me the importance of being a consistent, enthusiastic, energetic, and responsible scientist. It has been my pleasure to work with you. I would also like to thank Prof. Dr. Long Chen and Prof. Dr. German A. Enciso for agreeing to chair the dissertation committee.

There are a few more individuals I would like to thank who have been influential to me. I would like to thank Prof. Dr. Kuang Yang and Prof. Dr. Sebastien Motsch from Arizona State University, who set me on the path of mathematical biology and helped me build a solid foundation for my research career. I am also grateful to my uncle, Prof. Dr. Dongbin Xiu from Ohio State University. He sparked my passion for applied math since I was a teenager and provided guidance about careers in academia and industry.

Furthermore, I am sincerely grateful to my colleagues, classmates, friends and mentors in MCSB program and the Lowengrub group: Dr. Michelle Ngo, Dr. Matt Karikomi, Dr. Pavan Nayak, Dr. Neelakshi Soni, Dr. Lucas Ustick, Dr. Katiana Khouri, Dr. Shiji Zhao, Dr. Yanguang Chu, Dr. Daniel Ramirez-Guerrero and Dr. Abdon Iniguez for the numerous chats, discussions and assistant in my Ph.D. studies. Thank you for making work such a pleasant, productive, and friendly environment.

Special thanks to two former postdocs in the Lowengrub Lab: Dr. Zhenlin Guo and Dr. Huaming Yan. They have offered valuable guidance during my Ph.D. studies, helped me to implement efficient computer programs, and write rigorous mathematical proofs. Without their help, I wouldn't have been able to generate such a satisfying outcome in my work.

I would like to acknowledge the funding support from NIH U54 CA217378 01A1.

Outside the labs, I would like to thank all of my friends who have helped me in various ways over the years. I am lucky to have met all of them. Special thanks to Guanlin Li, Ziqi Sun, Haiming Zhang, and Ran Yin for the inspiring discussions and support regarding science and life. I'm also grateful to Sichi Chen, who taking the time to help me revise the article from an artistic perspective. Finally, none of this would have been possible without the encouragement and support of my parents, Yukun Tang and Yanbin Xiu, as well as my cat, Turing. Thank you all for always being there for me.

VITA

Weihao Tang

EDUCATION

Doctor of Philosophy in Mathematical, Computational and Systems Biology **2017-2024**
University of California Irvine *Irvine, CA*

Bachelor of Science in Computational Mathematics **2014-2017**
Arizona State University *Tempe, AZ*

RESEARCH EXPERIENCE

Graduate Research Assistant **2017–2024**
University of California, Irvine *Irvine, CA*

TEACHING EXPERIENCE

Teaching Assistant **2017–2023**
University of California, Irvine *Irvine, CA*

ABSTRACT OF THE DISSERTATION

Mathematical modeling of tumor growth and angiogenesis

By

Weihao Tang

Doctor of Philosophy in Mathematical, Computation and Systems Biology

University of California, Irvine, 2024

Professor John S. Lowengrub, Chair

Tumor angiogenesis plays a crucial role in cancer progression and metastasis. Mathematical modeling has emerged as a powerful tool to unravel the complex dynamics of tumor angiogenesis and to develop new therapeutic strategies. In this thesis, we focus on a comprehensive study on the mathematical modeling of tumor-induced angiogenesis, spanning from the fundamental concepts to the development of a novel hybrid model that integrates tumor growth and angiogenesis in a complex, realistic vascular network. We start from investigating a thermodynamically consistent mixture model for avascular solid tumor growth. To simulate tumor growth, we develop a mass-conservative, adaptive, finite difference, nonlinear multigrid method that captures the evolution of tumor morphology accurately and efficiently. Next, we present a hybrid model for angiogenesis growth based on the phase-field theory. The model incorporates the dynamics of capillaries, angiogenic factors, and tip endothelial cells (TECs), along with a discrete conceptualization of filopodia that enables TECs to sense their microenvironment. Finally, we build a mathematical model of tumor-induced angiogenesis that integrates tumor growth and angiogenesis in a complex, realistic vascular network extracted from the vascularized microtumor (VMT) platform. The model combines continuum and discrete modeling approaches to capture the key biological processes involved in tumor angiogenesis, and is simulated by our new developed numerical method.

Chapter 1

Introduction and Background

1.1 Introduction to cancer biology

Cancer is a major public health problem worldwide and one of the most fatal diseases of recent times that causes several deaths every year. Globally, more than 19.3 million new cancer cases were diagnosed and reported recently, leading to approximately 10 million deaths in 2020 based on the reported data [79]. By 2040, there will be 28 million new cases of cancer worldwide, leading to 16.3 million cancer-related deaths annually. Given the unique nature of cancer, the precise mechanisms that cause cancer are unclear and there is a lot of controversy over how exactly cancer is initiated.

The two groundbreaking studies, the key hallmarks of cancer, point out the relevance of genetic mutations in the development of cancers [48, 49]. As outlined by Hanahan and Weinberg, the key hallmarks of cancer were proposed as a set of functional capabilities acquired by human cells as they make their way from normalcy to neoplastic growth states, more specifically capabilities that are crucial for their ability to form malignant tumors. Initially, the hallmarks of cancer envisaged the complementary involvement of six distinct hallmark

capabilities and later expanded this number to eight. The eight hallmarks currently comprise the acquired capabilities for sustaining proliferative signaling, evading growth suppressors, resisting cell death, enabling replicative immortality, inducing/accessing vasculature, activating invasion and metastasis, reprogramming cellular metabolism, and avoiding immune destruction [47]. Cancer commonly begins with genetic mutations that lead to an enhanced proliferation rate and the formation of an avascular tumor. In normal tissues, healthy cells proliferate and divide according to the requirements of the organism. However, when cancer develops, the ability to regulate growth and maintain homeostasis is disrupted. With the accumulation of multiple changes, cells that should have grown old or damaged survive, and new cells form unnecessarily. These extra cells divide uncontrollably, leading to abnormal lumps called tumors.

1.2 The stages of solid tumor growth

There are three distinct stages (avascular, vascular, and metastatic) to cancer development. The first stage is the avascular stage where the cells receive nutrients and oxygen from existing blood vasculature. There is a balance between cells inside the tumor consuming nutrients and nutrient diffusion into the tumor [66].

Angiogenesis is the formation of new blood vessels from a preexisting vessel. It is also the process that tumors acquiring the ability develop their own blood supply from the host vasculature which is one of the most important steps in malignant tumor growth. Once vascularized, the tumor has access to enough nutrients, followed by rapidly growth[18]. Meanwhile, the tumor cells have the ability to escape the primary tumor via the circulatory system(metastasis) and set up secondary tumors elsewhere in the body. After angiogenesis and metastasis, the patient is left with multiple tumors in different parts of the body. These tumors are very difficult to detect and even more difficult to treat [76].

Over the course of several decades, researchers have turned to mathematical and computational models as essential tools for grasping and emulating tumor growth and various frameworks have emerged to elucidate the spatial dynamics of tumors and their microenvironment, spanning a spectrum of complexity levels. See the recent reviews by Lowengrub *et al.*[62], Yin *et al.*[94], Bekisz *et al.*[8], Humphrey *et al.*[55], and Metzcar *et al.* [65]

1.3 Mathematical modeling in cancer

Mathematical modeling has emerged as a powerful tool to better understand the dynamics of cancer progression, treatment response, and the development of novel therapeutic strategies [1]. These models aim to capture the key biological processes involved in cancer, such as cell proliferation, apoptosis, angiogenesis, and metastasis, using mathematical equations and computational simulations.

In recent years, various mathematical approaches have been employed to model different aspects of cancer. These include ordinary and partial differential equations, agent-based models, stochastic models, and hybrid models [36]. Evolutionary game theory has been applied to study the competition and cooperation among different tumor cell sub-populations [6]. Additionally, mathematical models have been used to optimize treatment schedules, predict patient outcomes, and design personalized therapies [5].

Despite the significant progress made in mathematical modeling of cancer, challenges remain in integrating the vast biological complexity and heterogeneity of tumors into tractable mathematical frameworks [89]. Future research will likely focus on developing multiscale models that bridge the gap between molecular, cellular, and tissue-level processes, as well as incorporating patient-specific data to enable personalized predictions and treatment optimization [75].

In light of these challenges and opportunities, this dissertation aims to contribute to the field of mathematical modeling of cancer by developing models and numerical methods that accurately and efficiently describe tumor evolution.

1.4 Outline

This thesis is organized as follows: In Chapter 2, we develop a mass-conservative, adaptive, finite difference, nonlinear multigrid method to simulate the progression of solid tumor growth using mixture models. After the mixture model is formulated, we discuss the details of numerical algorithm. Then, we present numerical simulations of tumor growth in 2D and 3D along with comparisons between mass-conservative and non-mass-conservative schemes. We incorporate stochastic effects to demonstrate the power of our numerical approach, in both 2D and 3D.

In Chapter 3, we investigate the dynamics of angiogenesis using a hybrid model. We discuss a multi-scale phase-field angiogenesis model that allows one to resolve capillaries at full time scale and to simulate long-term dynamics of angiogenesis. First, we introduce various components of the model, such as tumor angiogensis factor, capillaries, tip endothelial cells and filopodia. Then, Then, we discuss the numerical method to undertake the coupling between the discrete and continuous parts of the algorithm. Last, simulations are presented to study the development of angiogenesis from pre-existing vessel networks in the simple domain.

Building upon the foundations laid in Chapters 2 and 3, Chapter 4 presents a hybrid mathematical model that integrates tumor growth and angiogenesis in a complex, realistic vascular network extracted from the vascularized microtumor (VMT) platform. The model combines continuum and discrete modeling approaches to capture the key biological processes involved

in tumor angiogenesis.

Finally, a summary of the thesis and its contained works is provided in Chapter 5 along with directions for future studies and extensions.

Chapter 2

A Mass-conservative Adaptive Multigrid Algorithm for Simulating Solid Tumor Growth using Mixture Models

2.1 Introduction

The morphological evolution of a growing solid tumor is the result of the dynamics of a nonlinear, multiscale complex system. Over the course of several decades, researchers have turned to mathematical and computational models as essential tools for grasping and emulating tumor growth and various frameworks have emerged to elucidate the spatial dynamics of tumors and their microenvironment, spanning a spectrum of complexity levels. [43, 1, 4, 77, 9, 27, 41, 67, 73, 76]. See the recent reviews by Lowengrub *et al.*[62], Yin *et al.*[94], Bekisz *et al.*[8] , Humphrey *et al.*[55] , Metzcar *et al.* [65]

There are a variety of methods now available for performing nonlinear simulations of solid tumor growth. Most tumor models can be categorized into two general categories : continuous and discrete models [77]. The continuum approach considers the average of the global cell population behavior and tracks cell elements or volume fractions and is governed by PDE or integro differential equations [29, 28, 60, 68, 88, 91, 71]. The discrete approaches track and update individual cell dynamics using a prescribed set of biophysical rules[65, 83]. While discrete models may be good for targeting cell and sub-scale processes, they are fairly limited by rapidly increasing computational cost and studying analytically[83]. In larger-scale systems (millimeter to centimeter scale), continuum methods provide a good modeling alternative and mixture models provide the capability of simulating the interactions among multiple cell species, interstitial fluid and extracellular matrix [55, 77].

Continuum theories of mixtures, which provide a realistic representation of a tumor growing in a microenvironment, have been the focus of much research for many years[19]. In mixture models of tumor growth, the governing equations consist of mass and momentum balance equations for each species, interphase mass, and momentum exchange.

In this work, we simulate numerically a thermodynamically consistent mixture model for avascular solid tumor growth which takes into account the nonlinear effects of cell-to-cell adhesion, and taxis-inducing chemical and molecular species. The governing equations are of Cahn-Hilliard type [20] and can be viewed as a regularization of previous mixture models, e.g.[2, 19]. The equations are derived using mass-conservation equations for each component together with momentum equations and momentum exchange between components that are determined in a thermodynamically consistent way.

Fundamental challenges in solving these systems numerically include developing stable time integration methods that remove the numerical stiffness introduced by high-order (e.g., fourth order) spatial derivatives in the models, and accurately solving the equations for the evolving, complex tumor morphologies that emerge from the gain and loss of mass and

stresses induced by cancer cell proliferation and death (apoptosis), as well as the effect of a nonuniform microenvironment. To overcome these computational challenges, we have developed a numerical algorithm based on a novel mass-conservative two-grid full approximation storage (FAS) solver, which extends the algorithm developed by Feng et al. in [38] to time-dependent problems. The algorithm in [38] is essentially a standard adaptive full approximation storage (AFAS) scheme, but with a modification that comes in the form of a mass-conservative correction to the coarse-level force. This is facilitated by the introduction of so-called zombie variables, which are ghost variables on the coarse grid that lie under a fine grid refinement patch. The zombie variables are then used to create mass corrections to the coarse-level force functions. In this way, the standard smoothing, prolongation and restriction operations are independent of the flux-balancing procedure at the coarse-fine interface. Here, the new feature is that the time dependence of the equation requires the application of these techniques on the discrete solution at the previous time step but on the newly updated mesh. The application of this method to a mixture model of tumor growth is also new.

The paper is organized as follows. After the mixture model is formulated in Section 2, we discuss the details of numerical algorithm in Section 3. In section 4, numerical simulations of tumor growth in 2D and 3D are then presented, along with comparisons between mass-conservative and non-mass-conservative schemes. We then incorporate stochastic effects to demonstrate the power of our numerical approach, in both 2D and 3D. Conclusion and future works are discussed in Section 5.

2.2 Two component mixtures model: tissue and water

2.2.1 Nondimensionalization model formulation

In this section, we consider a local model of two-component mixtures consisting of tumor tissue and water [28]. The model takes into account cell proliferation in response to a diffusible nutrient, which represents the effects of all growth promoting factors, and chemotaxis of cells up nutrient gradients. Following [28], we nondimensionalize the system using the intrinsic taxis time scale and a nutrient diffusion length scale. The dimensionless variables are:

- ϕ, the volume fraction of solid tumor components.
- μ, the chemical potential.
- σ, the concentration of nutrient.

See [28] for a derivation and details.

The evolution equation for ϕ is the following Cahn-Hilliard-type reaction-diffusion equation:

$$\phi_t = \nabla \cdot (M(\phi)\nabla\mu) + \mathcal{P}\sigma\phi - \mathcal{A}\phi, \tag{2.1}$$

$$M(\phi) = \frac{1}{\epsilon}\phi^2, \tag{2.2}$$

$$\mu = \mathcal{G}^{-1}(f'(\phi - \epsilon^2\Delta\phi)) - \epsilon\mathcal{X}_\sigma\sigma, \tag{2.3}$$

where $\mathcal{P}$ is a nondimensional growth rate, $\mathcal{A}$ is a nondimensional cell death rate, $\mathcal{X}_\sigma$ is a nondimensional chemotaxis strength and $\mathcal{G}$ is a nondimensional measure of cell-cell adhesion interactions. Further, ϵ is a small parameter that characterizes the width of the tumor-host interface (e.g., strength of intermixing).

Since nutrient diffusion occurs on a much faster time scale (e.g., minutes) than the cell-proliferation time scale (e.g., day or more), the nutrient concentration can be governed by a quasi-steady diffusion-reaction equation. We assume the consumption of the nutrient to be proportional to the local nutrient concentration and cellular fraction. Thus, the nondimensional quasi-steady nutrient equation can be given as

$$0 = \nabla \cdot (D(\phi)\nabla\sigma) - \sigma\phi, \tag{2.4}$$

where

$$D(\phi) = \phi + \mathcal{D}(1-\phi), \tag{2.5}$$

and $\mathcal{D}$ is the ratio of the diffusion coefficients for the tumor and host tissue. The boundary conditions are given by:

$$\nabla\phi \cdot \mathbf{n} = \nabla\mu \cdot \mathbf{n} = 0 \quad \text{on} \quad \partial\Omega, \tag{2.6}$$

$$\sigma = 1 \quad \text{on} \quad \partial\Omega. \tag{2.7}$$

2.3 Details of the numerical algorithm

Due to the high order derivatives and the stiffness of our system Eqs. (2.1)-(2.4), we apply the Crank-Nicolson (CN) method for the temporal discretization and the finite difference method for the spatial discretization so that the scheme has second order accuracy in both time and space. To solve the nonlinear equations at the implicit time level, we apply a mass-conservative, adaptive, FAS (Full Approximation Storage) multigrid solver for the implementations. Our multigrid solver is based on the work by Feng et al. [38]. In their work, the standard FAS method is modified to correct the mass loss along the coarse-fine

grid interface (where the coarse grid borders the fine grid), and global mass conservation is guaranteed over the entire computational domain. However, the solver developed in [38] can guarantee mass conservation only for fully implicit schemes. Therefore, we extend the solver by adding a new feature that ensures mass conservation for semi-implicit schemes, including but not limited to the CN method. In the following, we first present the CN discretization in §2.3.1, and then show the finite difference discretization in §2.3.2, and finally demonstrate the mass conservation property of our solver in §2.3.3.

2.3.1 Semi-implicit discretizations

As an illustration, we use the following CN-like semi-implicit scheme applied to Eqs. (2.1)-(2.4):

$$\frac{\phi^{n+1}-\phi^n}{\Delta t} = \boldsymbol{\nabla}\cdot\Big(M(\phi)\boldsymbol{\nabla}\mu\Big)^{n+\frac{1}{2}} + s^{n+\frac{1}{2}}, \tag{2.8}$$

$$s^{n+\frac{1}{2}} = \mathcal{P}\ (\sigma\phi)^{n+\frac{1}{2}} - \mathcal{A}\ \phi^{n+\frac{1}{2}}, \tag{2.9}$$

$$\mu^{n+1} = \mathcal{G}^{-1}\Big(f'(\phi^{n+1}) - \epsilon^2\Delta\phi^{n+1}\Big) - \epsilon\mathcal{X}_\sigma\sigma^{n+1}, \tag{2.10}$$

$$0 = \boldsymbol{\nabla}\cdot\Big(D(\phi)\boldsymbol{\nabla}\sigma\Big)^{n+1} - (\sigma\phi)^{n+1}, \tag{2.11}$$

where $*^{n+\frac{1}{2}} = \frac{1}{2}(*^{n+1} + *^n)$, $(\phi^n, \mu^n, \sigma^n)$ are the solutions at time $t = n\Delta t$, Δt is the time step, and $M(\phi)$ and $D(\phi)$ are defined in Eqs. (2.2) and (2.5) respectively. Moreover, the boundary conditions are given by:

$$\boldsymbol{\nabla}\phi^n\cdot\mathbf{n} = \boldsymbol{\nabla}\mu^n\cdot\mathbf{n} = 0 \quad \text{on} \quad \partial\Omega, \tag{2.12}$$

$$\sigma^n = 1 \quad \text{on} \quad \partial\Omega. \tag{2.13}$$

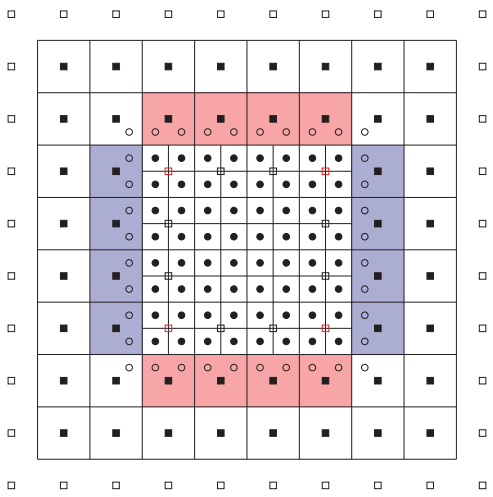

Figure 2.1: A simple two-level, "box-in-box" two-dimensional computational grid. The mesh sizes in this example are $m_0 = 8$ and $m_1 = 8$. The unfilled squares (circles) represent the locations of the ghost points for coarse (fine) grid. The cells contained in the four coarse-level strips (shaded red and blue) just outside of the fine level patch are indexed by the sets $\mathcal{I}^{\text{ns}}_{0\backslash 1}$ (red) and $\Omega^{\text{ns}}_{0\backslash 1}$ (blue), respectively.

2.3.2 Two-grid finite difference discretizations

We next show the two-grid finite difference discretizations. Here, we use a two-level adaptive mesh as an illustration. Note that in the implementation, the solver is not restricted to two-grid case, see [38] for more details. We consider a two-level composite mesh, denoted Ω_χ covering the domain $\Omega = (0, L_0)^2$. We assume that the root level uniform grid has size $m_\ell \times m_\ell \mid_{(\ell=0)} = m_0 \times m_0$ and mesh spacing $h_\ell \mid_{(\ell=0)} = h_0 = \frac{L_0}{m_0}$, where $\ell(= 0, 1)$ stands for the adaptive mesh level. In any case, the mesh spacing for the fine-level grid is invariably half that of the coarse grid, $h_\ell = \frac{h_{\ell-1}}{2}$, where $\ell \in \mathbb{N}^+$. Now, in the simplest possible case, we may have what appears in Fig. 2.1, where embedded in the center of this coarse mesh is a fine mesh of size $m_1 \times m_1$, where m_1 is even. For the box-in-box two-level mesh in Fig. 2.1, we have $m_0 = 8$ and $m_1 = 8$. However, everything that we describe can be generalized to more complicated two-level meshes, for example, those shown in Figs. 2.4 and 2.8.

In all cases, we let $\mathcal{I}_1$ be the index set of the cell-centered points of the cells contained in

the fine-level grid, denoted Ω_1. Similarly, let $\mathcal{I}_{0\backslash 1}$ be the index set of the cell-centered points for the collection of coarse-level cells, denoted $\Omega_{0\backslash 1}$, that are not covered by the fine grid. By $\mathcal{I}_{0\#1}$ we denote the index set for the cell-centered points of the coarse-grid cells, denoted $\Omega_{0\#1}$, that lie underneath the fine grid. Therefore, $\Omega_{0\backslash 1} \cup \Omega_{0\#1}$ stands for all the coarse-grid points.

For convenience of calculating the mass corrections, we define $\mathcal{I}^{\text{ew}}_{0\backslash 1}$ to be the index the cell-centered points of the collection of coarse-grid cells, $\Omega^{\text{ew}}_{0\backslash 1}$, that border the eastern and western boundaries of the fine grid. These cells are shaded blue in Fig. 2.1. Likewise, let $\mathcal{I}^{\text{ns}}_{0\backslash 1}$ be the index set for the cell-centered points of the set of coarse-grid cells, $\Omega^{\text{ns}}_{0\backslash 1}$, that border the northern and southern boundaries of the fine grid. These cells are shaded red in Fig. 2.1. Finally, we define

$$\Omega_{0\backslash\backslash 1} := \Omega_{0\backslash 1} - \left(\Omega^{\text{ew}}_{0\backslash 1} \cup \Omega^{\text{ns}}_{0\backslash 1}\right).$$

The index set for the cell-centered points of the cells in $\Omega_{0\backslash\backslash 1}$ is denoted as $\mathcal{I}_{0\backslash\backslash 1}$.

For concreteness, let us clearly identify the index sets for the simple box-in-box mesh (Fig. 2.1):

$$\begin{aligned}
\mathcal{I}_1 &= \left\{(i,j) \mid 1 \le i,j \le m_1\right\}, \\
\mathcal{I}_{0\#1} &= \left\{(i,j) \;\middle|\; m_0^0 + 1 \le i,j \le m_0^1\right\}, \\
\mathcal{I}_{0\backslash 1} &= \left\{(i,j) \mid 1 \le i,j \le m_0\right\} \setminus \mathcal{I}_{0\#1}, \\
\mathcal{I}^{\text{ew}}_{0\backslash 1} &= \left\{(i,j) \;\middle|\; i = m_0^0, m_0^1 + 1, \quad m_0^0 + 1 \le j \le m_0^1\right\}, \\
\mathcal{I}^{\text{ns}}_{0\backslash 1} &= \left\{(i,j) \;\middle|\; m_0^0 + 1 \le i \le m_0^1, \quad j = m_0^0, m_0^1 + 1\right\}, \\
\mathcal{I}_{0\backslash\backslash 1} &= \mathcal{I}_{0\backslash 1} - \left(\mathcal{I}^{\text{ew}}_{0\backslash 1} \cup \mathcal{I}^{\text{ns}}_{0\backslash 1}\right),
\end{aligned}$$

where m_0^0 stands for the coarse grid point that is adjacent to the fine grid from the left or the bottom, and m_0^1 stands for the coarse grid point that is adjacent to the fine grid from

the right or the top. In Fig. 2.1, $m_0^0 = 2$ and $m_0^1 = 6$.

We then show some basic definitions and notations for the finite difference discretization. In general, let $\Omega_\ell = (0, L_\ell)^2$ be the domain of the ℓth level adaptive mesh, with $L_\ell = m_\ell \times h_\ell$, we consider the following sets

$$C_{m_\ell} = \{x_{\ell,i} \quad | i = 1, ..., m_\ell\}, \tag{2.14}$$

$$C_{\bar{m}_\ell} = \{x_{\ell,i} \quad | i = 0, ..., m_\ell + 1\}, \tag{2.15}$$

$$E_{m_\ell} = \{x_{\ell,i+\frac{1}{2}} | i = 0, ..., m_\ell\}, \tag{2.16}$$

where the elements of C_{m_ℓ} and $C_{\bar{m}_\ell}$ are called cell-centered points, $x_{\ell,i} = (i - \frac{1}{2}) \times h_\ell$ and $C_{\bar{m}_\ell}/C_{m_\ell}$ are the ghost points. E_{m_ℓ} contains edge-centered points with $x_{\ell,i+\frac{1}{2}} = i \times h_\ell$. We then define the following function spaces:

$$C_{\bar{m}_\ell \times \bar{m}_\ell} = \{f_c : C_{\bar{m}_\ell} \times C_{\bar{m}_\ell} \to \boldsymbol{R}\}, \tag{2.17}$$

$$C_{m_\ell \times \bar{m}_\ell} = \{f_c : C_{m_\ell} \times C_{\bar{m}_\ell} \to \boldsymbol{R}\}, \tag{2.18}$$

$$C_{\bar{m}_\ell \times m_\ell} = \{f_c : C_{\bar{m}_\ell} \times C_{m_\ell} \to \boldsymbol{R}\}, \tag{2.19}$$

$$E^{ew}_{m_\ell \times \bar{m}_\ell} = \{u : E_{m_\ell} \times C_{\bar{m}_\ell} \to \boldsymbol{R}\}, \tag{2.20}$$

$$E^{ns}_{\bar{m}_\ell \times m_\ell} = \{v : C_{\bar{m}_\ell} \times E_{m_\ell} \to \boldsymbol{R}\}, \tag{2.21}$$

for cell-centered functions f_c: ϕ, μ and σ, and for east–west and north–south edge-centered functions or operators respectively. According to different variable locations, we define the average and difference operators as follows:

$$A_{\ell,x} \text{ and } D_{\ell,x} : C_{\bar{m}_\ell \times \bar{m}_\ell} \to E^{ew}_{m_\ell \times \bar{m}_\ell}, \tag{2.22}$$

$$A_{\ell,y} \text{ and } D_{\ell,y} : C_{\bar{m}_\ell \times \bar{m}_\ell} \to E^{ns}_{\bar{m}_\ell \times m_\ell}, \tag{2.23}$$

$$a_{\ell,x} \text{ and } d_{\ell,x} : E^{ew}_{m_\ell \times \bar{m}_\ell} \to C_{m_\ell \times \bar{m}_\ell}, \tag{2.24}$$

$$a_{\ell,y} \text{ and } d_{\ell,y} : E^{ns}_{\bar{m}_\ell \times m_\ell} \to C_{\bar{m}_\ell \times m_\ell}. \tag{2.25}$$

We also define the following composite operators for simplicity:

$$*_{\ell,A} = \begin{pmatrix} A_{\ell,x} & 0 \\ 0 & A_{\ell,y} \end{pmatrix}, \quad \boldsymbol{\nabla}_{\ell,D} = \begin{pmatrix} D_{\ell,x} \\ D_{\ell,y} \end{pmatrix},$$

$$*_{\ell,a} = \begin{pmatrix} a_{\ell,x} & 0 \\ 0 & a_{\ell,y} \end{pmatrix}, \quad \boldsymbol{\nabla}_{\ell,d} = (d_{\ell,x}, d_{\ell,y}), \quad \Delta_\ell = \boldsymbol{\nabla}_{\ell,d} \cdot \boldsymbol{\nabla}_{\ell,D}. \tag{2.26}$$

With the help of the above definitions, the two-grid finite difference discretizations for the Eqs. (2.8)-(2.13) can be given as the following: find $(\phi, \mu, \sigma)_{i,j}^{n+1} \in \mathcal{C}_{\bar{m}_\ell \times \bar{m}_\ell}$ by solving:

$$\frac{\phi_{i,j}^{n+1} - \phi_{i,j}^{n}}{\Delta t} = \boldsymbol{\nabla}_{\ell,d} \cdot \Big(M(\phi)_{\ell,A} \boldsymbol{\nabla}_{\ell,D}\ \mu \Big)_{i,j}^{n+\frac{1}{2}} + s_{i,j}^{n+\frac{1}{2}}, \tag{2.27}$$

$$s_{i,j}^{n+\frac{1}{2}} = \mathcal{P}\ (\sigma\phi)_{i,j}^{n+\frac{1}{2}} - \mathcal{A}\ \phi_{i,j}^{n+\frac{1}{2}}, \tag{2.28}$$

$$\mu_{i,j}^{n+1} = \mathcal{G}^{-1} \Big(f'(\phi) - \epsilon^2 \Delta_\ell \phi \Big)_{i,j}^{n+1} - \epsilon \mathcal{X}_\sigma \sigma_{i,j}^{n+1}, \tag{2.29}$$

$$0 = \boldsymbol{\nabla}_{\ell,d} \cdot \Big(D(\phi)_{\ell,A} \boldsymbol{\nabla}_{\ell,D}\ \sigma \Big)_{i,j}^{n+1} - (\sigma\phi)_{i,j}^{n+1}, \tag{2.30}$$

where $(\phi, \mu, \sigma)_{i,j}^{n} \in \mathcal{C}_{\bar{m}_0 \times \bar{m}_0}$ are the solutions at time $t = n\Delta t$, Δt is the time step, and $*^{n+\frac{1}{2}} = \frac{1}{2}(*^{n+1} + *^{n})$. In addition, $M(\phi)$ and $D(\phi)$ are defined in Eqs. (2.2) and (2.5) respectively. Moreover, the boundary conditions are given by:

$$D_{0,x}\ \phi_{\frac{1}{2},j}^{n} = D_{0,x}\ \mu_{m_0+\frac{1}{2},j}^{n} = 0 \quad \text{for} \quad 1 \le j \le m_0, \tag{2.31}$$

$$D_{0,y}\ \phi_{i,\frac{1}{2}}^{n} = D_{0,y}\ \mu_{i,m_0+\frac{1}{2}}^{n} = 0 \quad \text{for} \quad 1 \le i \le m_0, \tag{2.32}$$

$$A_{0,x}\ \sigma_{\frac{1}{2},j}^{n} = A_{0,x}\ \sigma_{m_0+\frac{1}{2},j}^{n} = 1 \quad \text{for} \quad 1 \le j \le m_0, \tag{2.33}$$

$$A_{0,y}\ \sigma_{i,\frac{1}{2}}^{n} = A_{0,y}\ \sigma_{i,m_\ell+\frac{1}{2}}^{n} = 1 \quad \text{for} \quad 1 \le i \le m_0. \tag{2.34}$$

2.3.3 Mass conservation

As discussed in [38], the mass fluxes of the diffusion terms are not balanced at the coarse-fine grid interfaces, we need to find the ghost points and the mass change at coarse-fine grid interfaces to ensure mass conservation on the adaptive grid. Conventional wisdom suggests that a relatively higher order interpolation is normally needed for the ghost variables along the coarse-fine grid interface on a composite mesh so that global second-order accuracy can be maintained. For example, cubic interpolation is employed in [15, 63], for the composite mesh in 2D. Only with very careful treatment along the coarse-fine grid interfaces [63, 69] can the method conserve mass. In [38], the standard FAS multigrid solver is modified such that even the combination of (low-order) linear interpolation paired with flux-balancing is sufficient to maintain global second-order accuracy and mass conservation. However, the solver is only restricted to fully implicit schemes. Here we extend their work by adding a new feature such that the mass conservation for diffusion equations can be preserved for semi-implicit schemes. For simplicity, we use Eq. (2.27) as an illustration. We first rewrite Eq. (2.27) into the flux form:

$$\begin{aligned}\frac{\phi_{i,j}^{n+1}-\phi_{i,j}^{n}}{\Delta t} &= \boldsymbol{\nabla}_{\ell,d}\cdot\left(M(\phi)_{\ell,A}\boldsymbol{\nabla}_{\ell,D}\ \mu\right)_{i,j}^{n+\frac{1}{2}} + s_{i,j}^{n+\frac{1}{2}} \\ &= \left(\frac{F^{\mathrm{ew}}_{\ell,i+\frac{1}{2},j}-F^{\mathrm{ew}}_{\ell,i-\frac{1}{2},j}}{h_\ell}+\frac{F^{\mathrm{ns}}_{\ell,i,j+\frac{1}{2}}-F^{\mathrm{ns}}_{\ell,i,j-\frac{1}{2}}}{h_\ell}\right)^{n+\frac{1}{2}} + s_{i,j}^{n+\frac{1}{2}},\end{aligned} \tag{2.35}$$

where we define the fluxes:

$$\begin{aligned}F^{\mathrm{ew}}_{\ell,i+\frac{1}{2},j} &= -(A_{\ell,x}M)_{i+\frac{1}{2},j}\ \frac{\mu_{\ell,i+1,j}-\mu_{\ell,i,j}}{h_\ell} = -M^{\mathrm{ew}}_{\ell,i+\frac{1}{2},j}\frac{\mu_{\ell,i+1,j}-\mu_{\ell,i,j}}{h_\ell}, \\ F^{\mathrm{ns}}_{\ell,i,j+\frac{1}{2}} &= -(A_{\ell,y}M)_{i,j+\frac{1}{2}}\frac{\mu_{\ell,i,j+1}-\mu_{\ell,i,j}}{h_\ell} = -M^{\mathrm{ns}}_{\ell,i,j+\frac{1}{2}}\frac{\mu_{\ell,i,j+1}-\mu_{\ell,i,j}}{h_\ell},\end{aligned} \tag{2.36}$$

for $*^{ew} \in E^{ew}_{m_\ell}$, $*^{ns} \in E^{ew}_{m_\ell}$, $\ell = 0, 1$, and $(i,j) \in \mathcal{I}_{0\setminus 1}$ when $\ell = 0$, and $(i,j) \in \mathcal{I}_1$ when $\ell = 1$. The discrete homogeneous Neumann boundary conditions are enforced on the physical

boundary:

$$F^{\text{ew}}_{0,0+\frac{1}{2},j} = F^{\text{ew}}_{0,m_0+\frac{1}{2},j} = 0, \quad j = 1, \cdots, m_0, \tag{2.37}$$

$$F^{\text{ns}}_{0,i,0+\frac{1}{2}} = F^{\text{ns}}_{0,i,m_0+\frac{1}{2}} = 0, \quad i = 1, \cdots, m_0. \tag{2.38}$$

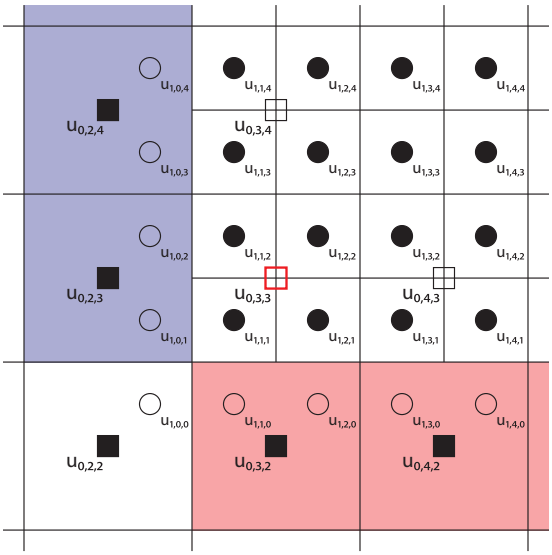

Figure 2.2: Variable numbering scheme near the lower left double zombie point, shown in red. This is a close-in view of the composite grid shown in Fig. 2.1.

In our solver, all the ghost points are obtained by using linear interpolations (**LIF** method, see [38] for details), under which case the mass fluxes of the diffusion term are not balanced at the coarse-fine grid interface. For simplicity, we use the mesh shown in Fig. 2.2 as an example. For the point $(\ell = 0, i = 2, j = 3)$ on the coarse grid, we have the unbalanced mass fluxes:

$$h_0 F^{\text{ew}}_{0,2+\frac{1}{2},4} \neq h_1 F^{\text{ew}}_{1,0+\frac{1}{2},3} + h_1 F^{\text{ew}}_{1,0+\frac{1}{2},4}. \tag{2.39}$$

To enforce mass conservation, we first calculate the mass change at that point:

$$C^{ew}_{0,2,3} = h_0 F^{\text{ew}}_{0,2+\frac{1}{2},4} - h_1 F^{\text{ew}}_{1,0+\frac{1}{2},3} - h_1 F^{\text{ew}}_{1,0+\frac{1}{2},4}, \tag{2.40}$$

we then insert this correction term as an extra source term to Eq. (2.35) for the corresponding point on the mesh level $\ell = 0$ to ensure local mass conservation. In general the mass corrections on the coresponding coarse points can be given by

$$\text{for} \quad j \in \mathcal{I}^{\text{ew}}_{0\setminus 1}, \;\; \bar{j} = 1, ..., m_1/2 :$$

$$C^{ew}_{0,m^0_0,j} = h_0 F^{\text{ew}}_{0,m^0_0,j} - h_1 (F^{\text{ew}}_{1,0+\frac{1}{2},2\bar{j}-1} - F^{\text{ew}}_{1,0+\frac{1}{2},2\bar{j}}), \tag{2.41}$$

$$C^{ew}_{0,m^1_0,j} = -h_0 F^{\text{ew}}_{0,m^1_0,j} + h_1 F^{\text{ew}}_{1,m^1_1+\frac{1}{2},2\bar{j}-1} + h_1 F^{\text{ew}}_{1,m^1_1+\frac{1}{2},2\bar{j}}, \tag{2.42}$$

$$\text{for} \quad i \in \mathcal{I}^{\text{ns}}_{0\setminus 1}, \;\; \bar{i} = 1, ..., m_1/2 :$$

$$C^{ns}_{0,i,m^0_0} = h_0 F^{\text{ns}}_{0,i,m^0_0} - h_1 F^{\text{ns}}_{1,2\bar{i}-1,0+\frac{1}{2}} - h_1 F^{\text{ns}}_{1,1,2\bar{i},0+\frac{1}{2}}, \tag{2.43}$$

$$C^{ns}_{0,i,m^1_0} = -h_0 F^{\text{ns}}_{0,i,m^1_0} + h_1 F^{\text{ns}}_{1,2\bar{i}-1,m_1+\frac{1}{2}} + h_1 F^{\text{ns}}_{1,2\bar{i},m_1+\frac{1}{2}}. \tag{2.44}$$

We then insert these correction terms as extra source to Eq. (2.35) to obtain the two-grid, mass conservative finite difference discretization for Eq. (2.27)

$$\begin{aligned}\frac{\phi^{n+1}_{i,j} - \phi^n_{i,j}}{\Delta t} = &\left(\frac{F^{\text{ew}}_{0,i+\frac{1}{2},j} - F^{\text{ew}}_{\ell,i-\frac{1}{2},j}}{h_0} + \frac{F^{\text{ns}}_{\ell,i,j+\frac{1}{2}} - F^{\text{ns}}_{\ell,i,j-\frac{1}{2}}}{h_0} \right)^{n+\frac{1}{2}} + s^{n+\frac{1}{2}}_{i,j} \\ &+ \delta^{ew}_0 (C^{ew}_{0,m^0_1,j})^{n+\frac{1}{2}} + \delta^{ew}_1 (C^{ew}_{0,m^1_0,j})^{n+\frac{1}{2}} \\ &+ \delta^{ns}_0 (C^{ns}_{0,i,m^0_0})^{n+\frac{1}{2}} + \delta^{ns}_1 (C^{ns}_{0,i,m^1_0})^{n+\frac{1}{2}},\end{aligned} \tag{2.45}$$

where

$$\delta^{ew}_0 = \begin{cases} 1, \text{ if } \ell = 0 \;\&\; i = m^0_0 \;\&\; j \in \mathcal{I}^{\text{ew}}_{0\setminus 1}, \\ 0, \text{ otherwise}, \end{cases} \tag{2.46}$$

$$\delta_1^{ew} = \begin{cases} 1, \text{ if } \ell = 0 \ \& \ i = m_0^1 \ \& \ j \in \mathcal{I}_{0\setminus 1}^{\text{ew}}, \\ 0, \text{ otherwise,} \end{cases} \tag{2.47}$$

$$\delta_0^{ns} = \begin{cases} 1, \text{ if } \ell = 0 \ \& \ i \in \mathcal{I}_{0\setminus 1}^{\text{ns}} \ \& \ j = m_0^0, \\ 0, \text{ otherwise,} \end{cases} \tag{2.48}$$

$$\delta_1^{ns} = \begin{cases} 1, \text{ if } \ell = 0 \ \& \ i \in \mathcal{I}_{0\setminus 1}^{\text{ns}} \ \& \ j = m_0^1, \\ 0, \text{ otherwise.} \end{cases} \tag{2.49}$$

The above method is then solved by using the FAS multigrid solver presented in [38], where the difference is that the current discretizations contains the mass correction for the semi-implicit scheme.

The adaptive process is comprised of two basic steps: starting with a multilevel, block-structured mesh on which we have a computed solution, we (i) construct a new multilevel, block-structured mesh, and (ii) solve the problem on the new mesh using the adaptive version of the FAS multigrid method. New grids must be populated with data from the old mesh. We assume that two fine grids, one old and one new, live simultaneously, where the field variables are to be transferred from old to new. Both fine grids share the same parent grid, the root grid. Data from the old root-level grid are copied into the new root-level grid. Cell-centered data contained in the overlap of the old and new fine grids are simply copied. The fine data in the old grid that are not in the overlap are averaged and copied to the new root grid. The data in the new fine grid located where there is no overlap with an old fine grid must be generated by interpolation from the cell-centered data in the root grid. See [90] for more details.

2.4 Numerical results

2.4.1 2D spherically symmetric mass conservative tumor growth

We first investigate a two-dimensional simulation of a tumor growing into a nutrient-poor environment with $D = 1$. Assuming cell proliferation rate and cell apoptosis are extremely small, we set $\mathcal{P} = 0$ and $\mathcal{A} = 0$. We focus on the parameters $\epsilon = 0.01$, $D = 1$, and $\mathcal{X}_\sigma = 10$ (large nutrient taxis). The grid parameters are the following: the domain is $\Omega = (0, 25.6) \times (0, 25.6)$ with a root level grid of size 32^2. Five levels of refinement are used so that the finest level has the effective resolution of a uniform grid 1024×1024. Moreover, we set the time step $\Delta t = 1.0 \times 10^{-4}$. The initial tumor shape for the simulation is a slightly elliptical mass with a diffuse interface. The $\phi = 0.5$ level curve is given by

$$\{(x, y) | (\frac{x - 12.8}{2.1})^2 + (\frac{y - 12.8}{1.9})^2 = 1\} \tag{2.50}$$

In Fig. 2.3, three sets of simulations are computed by using the fully mass-conservative scheme, the non-mass-conservative scheme, and the standard finite difference scheme on uniform grid with equivalent effective mesh resolution. The evolution of the contours $\phi = 0.5$, together with the adaptive mesh are shown in Fig. 2.4. Here, the results of different schemes are very similar. The tumor grows rapidly and develops an annular morphology as it expands where tumor cells lie only in the annular region. Since the cell proliferation rate and cell apoptosis rate are negligible, the mass of tumor cells is conserved but the volume fraction near the center drops below the spinodal point (the point where $d^2 f / d^2 \phi$ changes sign) because of increased cell death at the center due to the lack of nutrient. This creates a cell-free zone in the center. As can be seen in Fig. 2.5, the nutrient concentration level near the center is almost 0. The annular, or ring-like structure, is formed because the tumor cells can not redistribute fast enough to maintain a uniform density due to the chemotaxis, low

cell mobility, and cell-cell adhesion that pulls the cells from the inner region toward the more nutrient-dense periphery. In Fig. 2.6, the total mass and surface area of tumor cells versus time are plotted. Mass is indeed conserved by our new scheme. The surface area evolves non-monotonically, but generally increases.

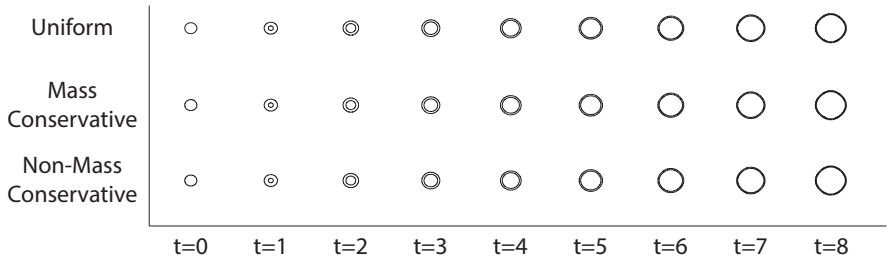

Figure 2.3: Evolution of tumor in 2D with $\mathcal{P} = 0$, $\mathcal{A} = 0$, $\epsilon = 0.01$, $D = 1$, $\mathcal{X}_\sigma = 10$, and initial tumor surface as in Eq. (2.50). The $\phi = 0.5$ contour are based on uniform grid, mass conservative scheme and non-mass conservative scheme.

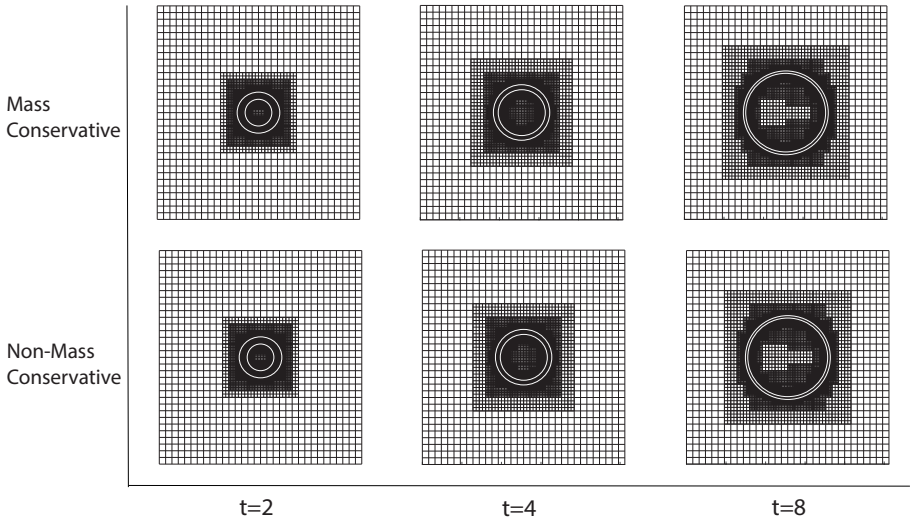

Figure 2.4: Evolution of the contours $\phi = 0.5$, together with four levels adaptive mesh, during growth.

We then consider the morphological evolution of tumors with a smaller interface thickness $\epsilon = 0.005$. All other parameters are the same as in the previous case. A smaller interface thickness implies a larger cell mobility via Eq. (2.2). Therefore, more tumor cells are able to reach the center. The tumor volume fraction near the center is higher than that with

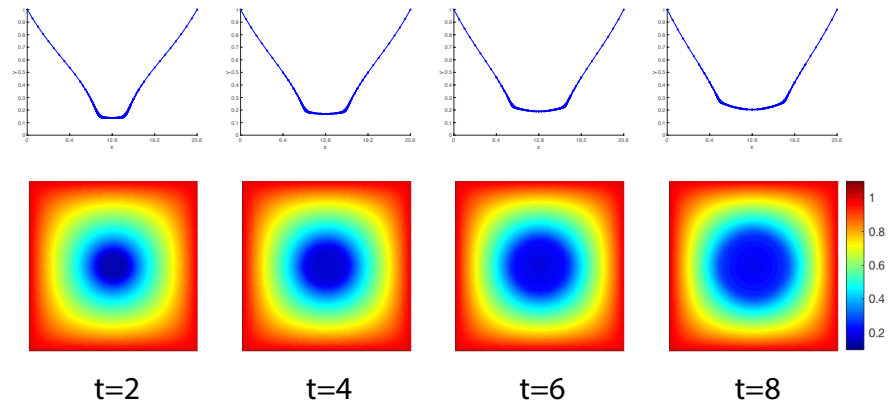

Figure 2.5: Up: 1D slice of nutrient concentration evolution at $y = 12.8$. Down: Contour plots of nutrient concentration evolution corresponding to the simulation.

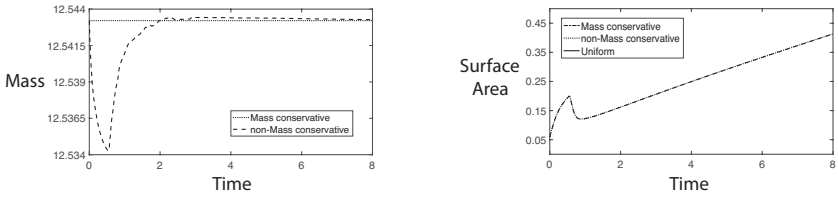

Figure 2.6: The comparison between the mass-conservative scheme and the non-mass-conservative scheme. Left: total mass. Right: surface area.

a smaller cell mobility, and therefore the tumor avoids forming a ring. Meanwhile, as ϵ is reduced (from 0.01 to 0.005), the thickness of the diffuse interfacial region is reduced. Hence, five levels of refinement are used to ensure that there are enough mesh points to resolve the tumor interface. The mesh here has an effective resolution of a uniform grid 1024×1024.

In Fig. 2.7, the dynamics of tumor simulations obtained on the adaptive mesh with the fully mass-conservative scheme and the non-mass-conservative scheme are depicted, along with the standard finite difference scheme on a uniform 1024^2 grid as the true solution for comparison. We observe that the tumor starts to generate fingering patterns at $t = 3$, increasing the surface area of the tumor and allowing better access to nutrient. At later times, the fingers continue to stretch out and branched network-like pattern emerges. At time $t = 8$, the non-mass conservative method is not able to simulate the thin fingers accurately, and eventually the fingers become detached. The evolution of the contours $\phi =$

0.5, together with the adaptive mesh are shown in Fig. 2.8. We remark that, because of its mass conservation property, our mass-conservative scheme visibly outperforms the non-mass conservative scheme. In Fig. 2.9, comparisons of the total mass and surface area confirm this.

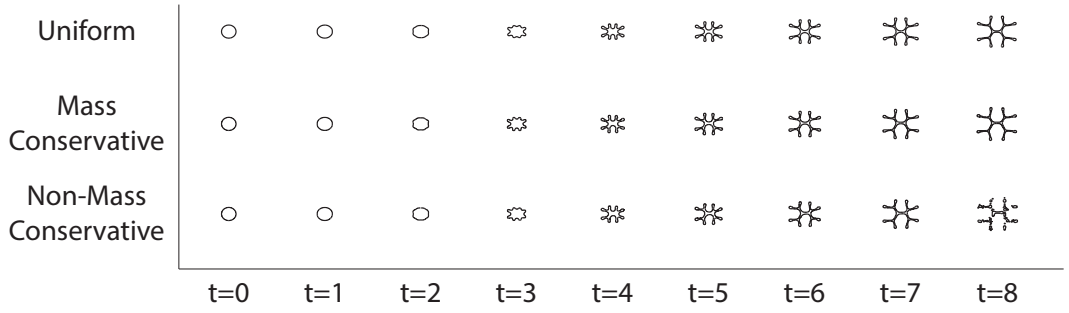

Figure 2.7: Evolution of tumor in 2D with $\mathcal{P} = 0$, $\mathcal{A} = 0$, $\epsilon = 0.005$, $D = 1$, $\mathcal{X}_\sigma = 10$, and initial tumor surface as in Eq. (2.50). The $\phi = 0.5$ contour are based on uniform grid, mass conservative solver and non-mass conservative solver.

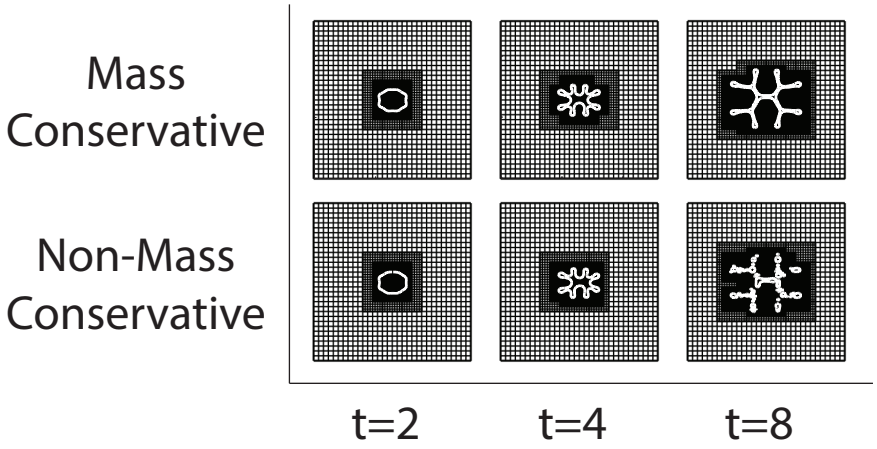

Figure 2.8: Evolution of the contours $\phi = 0.5$, together with five levels adaptive mesh, during growth.

We now investigate tumor growth into a nutrient-poor microenvironment with a low proliferation rate, $\mathcal{P} = 0.1$. The other parameters are taken to be $\mathcal{X}_\sigma = 5$ and $\epsilon = 0.01$, with four levels of mesh refinement. In Fig. 2.10, we observe that fingers develop, elongate, and form long, slim and invasive fingers at time $t = 15$. In Fig. 2.11, we zoom in on the results at time $t = 20$. Again, by comparing the results with those using a uniform mesh, we observe

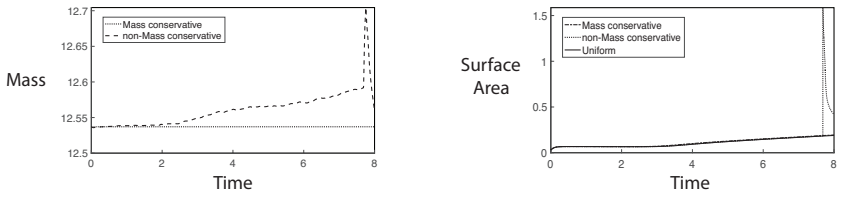

Figure 2.9: The comparison between the mass-conservative scheme and the non-mass-conservative scheme. Left: total mass. Right: surface area.

that the mass-conservative scheme is more accurate than the standard non-mass-conservative scheme.

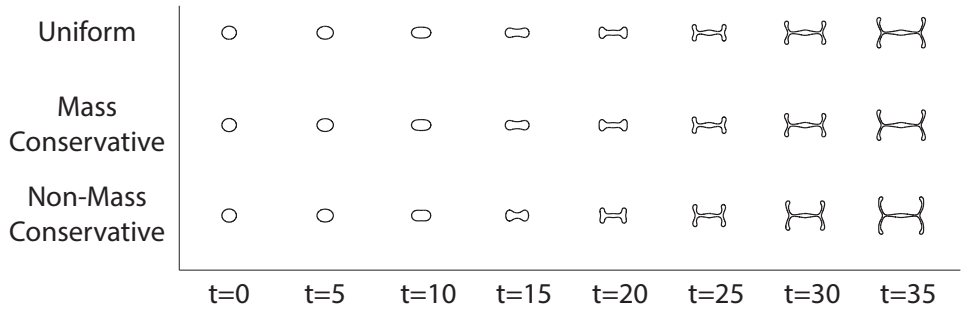

Figure 2.10: Evolution of tumor in 2D with $\mathcal{P} = 0.1$, $\mathcal{A} = 0$, $\epsilon = 0.01$, $D = 1$, $\mathcal{X}_\sigma = 5$, and initial tumor surface as in Eq. (2.50). The $\phi = 0.5$ contour are based on uniform grid, mass conservative scheme and non-mass conservative scheme.

2.4.2 Convergence test

To show our method is second order accurate both in time and space, we carry out a convergence test by considering the Cauchy sequence. We compute our scheme with the same initial condition, computational domain and parameters as the simulation case in Fig.3

We save the data produced by the adaptive algorithm on an uniform grid 1024×1024 using linear interpolation, and then perform a time-step refinement test to obtain the order of convergence in time by taking a linear refinement path for time step $\Delta t = 0.002/2^k$ for $k = 0, ..., 6$. The numerical errors are calculated as the difference between the solution of

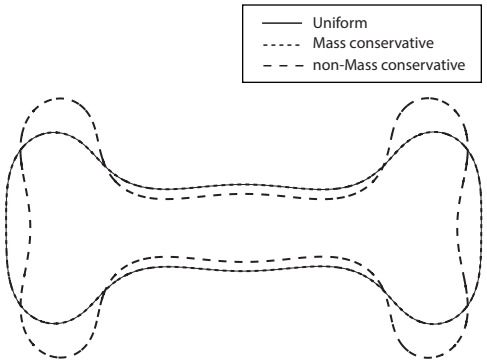

Figure 2.11: Zoom in the time $t = 20$ of Fig. 2.10.

Δt	$error_\phi$	$rate$
2.0×10^{-3}	1.44×10^{-2}	-
1.0×10^{-3}	7.2×10^{-3}	1.9997
5.0×10^{-4}	3.7×10^{-3}	1.9591
2.5×10^{-4}	1.9×10^{-3}	1.9845
1.25×10^{-4}	9.35×10^{-4}	1.9865
6.25×10^{-5}	4.73×10^{-4}	1.9780
3.125×10^{-5}	2.37×10^{-4}	1.9943

Table 2.1: The L^2 errors of the phase field variable ϕ obtained at t = 1 with different time step Δt.

coarse time step and that of the adjacent finer time step. We show the Cauchy sequence of L^2 errors at $t = 1$ with different time step sizes in Table 2.1, indicating a second order convergence rate in time.

To compare solutions on different grids, we refine the mesh according to the rule $m = 2^k$ for $k = 5, 6, 7, 8, 9$, where m is the number of grid points in both x direction and y direction. Then, we interpolate the solution at the coarse grid up to the next fine grid to calculate the difference in L^2 norm. We show the Cauchy sequence of L^2 errors at $t = 1$ with different mesh grid points in Table 2.2. The convergence rate shows that our numerical method is second order accurate.

m	$error$	$rate$
32&64	4.72×10^{-2}	-
64&128	2.86×10^{-2}	1.6490
128&256	1.45×10^{-2}	1.9787
256&512	7.23×10^{-3}	1.9964
512&1024	3.61×10^{-3}	1.9957

Table 2.2: The L^2 errors of the phase field variable ϕ obtained at t = 1 with different mesh grid points m.

2.4.3 Performance of the solver in three dimensions

Here, we present three-dimensional simulations of tumor growth. Note that $\epsilon = 0.005$ is used in Fig. 2.12-2.13. The other biophysical parameters are the same as those used in the first two-dimensional case, (Fig. 2.7). The initial tumor surface is

$$(\frac{x-12.8}{2.1})^2 + (\frac{y-12.8}{1.9})^2 + (\frac{z-12.8^{\,2}}{1.9}) = 1, \tag{2.51}$$

and the computational domain is $\Omega = (0, 25.6)^3$ with a root level grid of size 32^3. Four levels of mesh refinement are used so that the finest level has the effective resolution of a uniform grid $512 \times 512 \times 512$. The evolution of the $\phi = 0.5$ isosurface generated by the mass-conservative scheme is shown in Fig. 2.12, along with the slice of $\phi = 0.5$ at $x = 12.8$. Unlike its two-dimensional counterpart, the three-dimensional tumor does not form fingers and there is no tumor at center. The tumor interior becomes hollow and moves outward due to the chemotaxis, low cell mobility, weak adhesion forces, and the limited nutrient supply. The corresponding total mass and surface area comparisons are shown in Fig. 2.13. We observe that the total mass of the mass-conservative scheme is constant and the surface area increases but evolves non-monotonically.

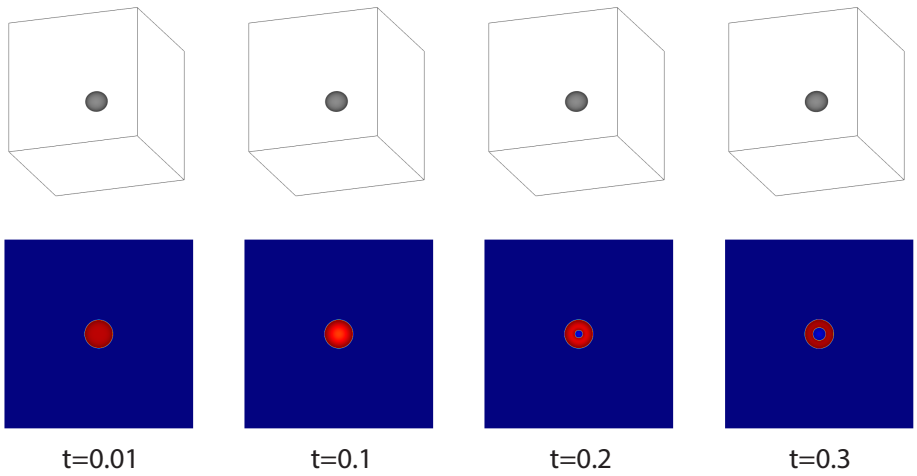

Figure 2.12: Up: The evolution of the $\phi = 0.5$ isosurface during the growth of a symmetrical 3D tumor with $\mathcal{P} = 0$, $\mathcal{A} = 0$, $\epsilon = 0.005$, $D = 1$, $\mathcal{X}_\sigma = 10$. Down: The slice of $\phi = 0.5$ isosurface at $x = 12.8$.

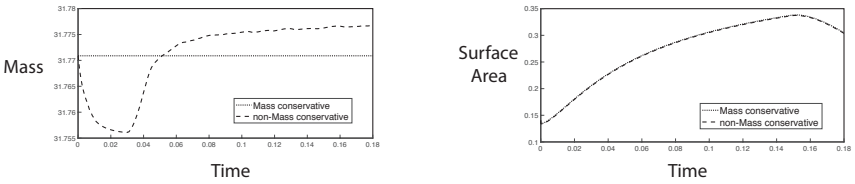

Figure 2.13: The comparison between the mass-conservative scheme and the non-mass-conservative scheme. Left: total mass. Right: surface area.

2.4.4 Tumor growth with stochastic effects

As another example of the power of our numerical approach, we investigate tumor growth with stochastic effects and a low proliferation rate, $\mathcal{P} = 0.1$. We further assume that the cell death rate is small, $\mathcal{A} = 0$. Thus, taxis dominates the cell dynamics. The other parameters are taken to be $\epsilon = 0.01$ and $D = 1$, $\mathcal{X}_\sigma = 5$. An adaptive mesh is used where the root level is 32×32 and four levels of mesh refinement are used to get the effective resolution of a uniform grid 512×512. We set the time step $\Delta t = 1 \times 10^{-3}$. As a simple model of biological noise and variability, consider the nutrient uptake to be a stochastic variable. In particular, the nutrient diffusion equation Eq. (2.4) is replaced by

$$0 = \nabla \cdot (D(\phi)\nabla\sigma) - \lambda\sigma\phi \tag{2.52}$$

where λ is a truncated normally distributed random variable in space, with mean $= 1$ that is bounded in $[0, 2]$. The variable λ is changed every 200 time steps. In Fig. 2.14, the results are shown during growth. The initial asymmetrical tumor shape for the simulation is displayed at time $t = 0$. It is clearly seen that the tumor acquires a highly complex spatial structure, branches and forms a dense network.

In our last example, we present a three-dimensional tumor growth simulations with stochastic effects. The parameters are the same as the previous two-dimensional simulation with stochastic effects. In Fig. 2.15, as in the two-dimensional case, the tumor develops a highly complex morphology.

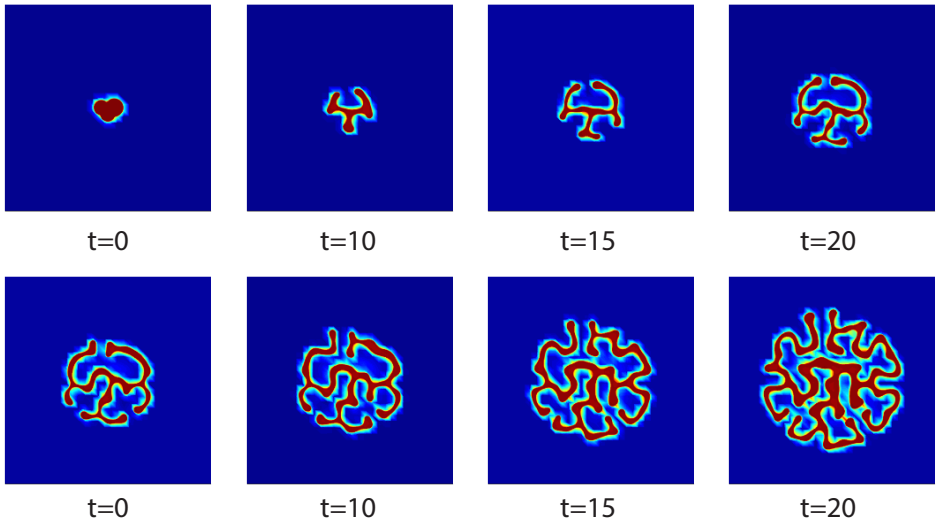

Figure 2.14: The evolution of an asymmetrical 2D tumor with stochastic effects. The parameters are : $\mathcal{P} = 0.1$, $\mathcal{X}_\sigma = 5$, $\epsilon = 0.01$.

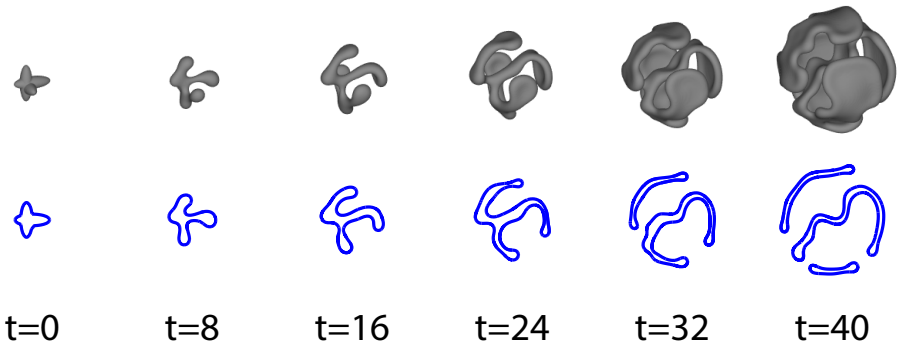

Figure 2.15: Evolution of the $\phi = 0.5$ isosurface and during the growth of an asymmetrical 3D tumor with stochastic effects. The parameters are: $\mathcal{P} = 0.1$, $\mathcal{X}_\sigma = 5$, $\epsilon = 0.01$.

2.5 Summary and future work

In this work, we simulated numerically a thermodynamically consistent mixture model for avascular solid tumor growth which was presented in [28]. The governing equations are Cahn-Hilliard type that takes into account cell proliferation and death, the effects of cell-to-cell adhesion, taxis inducing chemical and molecular species.

To solve the governing equations, the Crank-Nicolson (CN) method was used for the temporal discretization so that the scheme was second order accurate in time and a finite difference method was used for the spatial discretization to guarantee the second order accurate in space. We developed a novel mass-conservative two-grid full approximation storage (FAS) solver which extends the algorithm developed by Feng et al. in [38] to time-dependent problems. We also extended the solver by adding a new feature that the mass can be preserved for the semi-implicit scheme, including but not restricted to the CN method. The algorithm is essentially a standard adaptive full approximation storage (AFAS) scheme, but with a simple modification that comes in the form of a mass-conservative correction to the coarse-level force. This is facilitated by the introduction of what we call a zombie variable, analogous to a ghost variable, but defined on the coarse grid, and lying under a fine grid refinement patch. To maintain global mass conservation, we need only modify the usual FAS algorithm by correcting the coarse-level force function at points adjacent to the coarse-fine interface.

We presented tumor evolutions in nutrient-poor tissues with different mobility in 2D and 3D. The results shows that the mobility may drive fingering instabilities if it is large enough, otherwise the tumor forms an annular ring structure. To show our scheme, we compared our results with the simulations of the standard finite difference scheme on uniform grid which is automatically mass conserved. We also presented simulations of tumor growth with stochastic effects in 2D and 3D that demonstrate the capabilities of the algorithm simulating

the progression of tumors with complex morphologies.

In the future, we plan to extend the algorithm to incorporate more cells types and more physiological effects via tumor mixture models [93]. Eventually, we plan to develop a new multiscale model of vascular solid tumor growth which couples both tumor growth and angiogenesis models [87]. This is the subject of ongoing work.

Chapter 3

Mathematical Modeling of Angiogenesis

3.1 Introduction

Angiogenesis is a physiological and natural phenomenon by which new blood vessels emerge from an existing vascular system. It was discovered nearly a century ago that angiogenesis happens in the vicinity of tumors. It is essential to the regular processes involved in arthritis, wound healing, and solid tumor growth.

Hypoxia inducible factor (HIFα) is activated by a drop in local oxygen levels, which in turn stimulates the transcription and synthesis of angiogenic factors like vascular endothelial growth factor (VEGF)-A, thereby initiating angiogenesis.[80]. These pro-angiogenic factors diffuse outward from the hypoxic regions and eventually reach the neighboring blood vessels. After being discovered by the ECs, pro-angiogenic factors begin secreting matrix degrading enzymes that degrade the basement membrane and the extracellular matrix (ECM). Subsequently, ECs are activated to form tip endothelial cells (TECs), which become the leading

edge of a new sprouting vessel [34]. Directly behind the TECs are stalk cells that proliferate, elongate and form a local basement membrane [59]. They eventually align and surround a vascular lumen with tubes of polarized ECs. The blood vasculature grows and is extended when new or preexisting vessels unite through anastomosis.

Furthermore, during angiogenesis, VEGF and Notch signaling pathways are involved in the differentiation of TECs in the vascular endothelium. Under the stimulation of VEGF, the expression of Delta-like ligand 4 (Dll4) is up-regulated in TECs. Dll4 binds to Notch receptors of nearby endothelial cells which, in turn, reduces their VEGF receptor expression, consequently suppressing their TEC phenotype. See [13, 50] for more details.

Experimental evidence shows that vessels grow led by TECs [31]. TECs migrate mainly following the gradient of Hypoxia inducible factors (HIFα) and also facilitated by filopodia [51]. Filopodia are rod-like cell surface projections filled with bundles of parallel actin filaments that function as antennae for TECs to probe their microenvironment [64, 37], shown in Fig. 3.1. In particular, when filopodia sense the remnants of basement membrane, TECs alter their direction towards them to use them as the path of minimum resistance in their migration. Then, the vessels link with the old ones and form a network of loops during a process called *anastomosis*. Filopodia-based sensing plays a major role in anastomosis and loop formation and that chemotaxis itself is not enough to create connected networks that favour blood flow and oxygenation. The resulting neovasculature provides the hypoxic region with a direct supply of oxygen and other nutrients.

In the last few years, new or augmented mathematical models of angiogenesis have been developed and vary in the extent of biological details they characterize. Most of them can be summarized into three general categories: discrete, continuous and hybrid models (see Fig. 3.2). In discrete models, endothelial cells and vasculature are treated as individual objects. The vasculature develops through time based on sets of rules dictating cell behavior. Discrete models can resolve some local features but become computationally expensive as

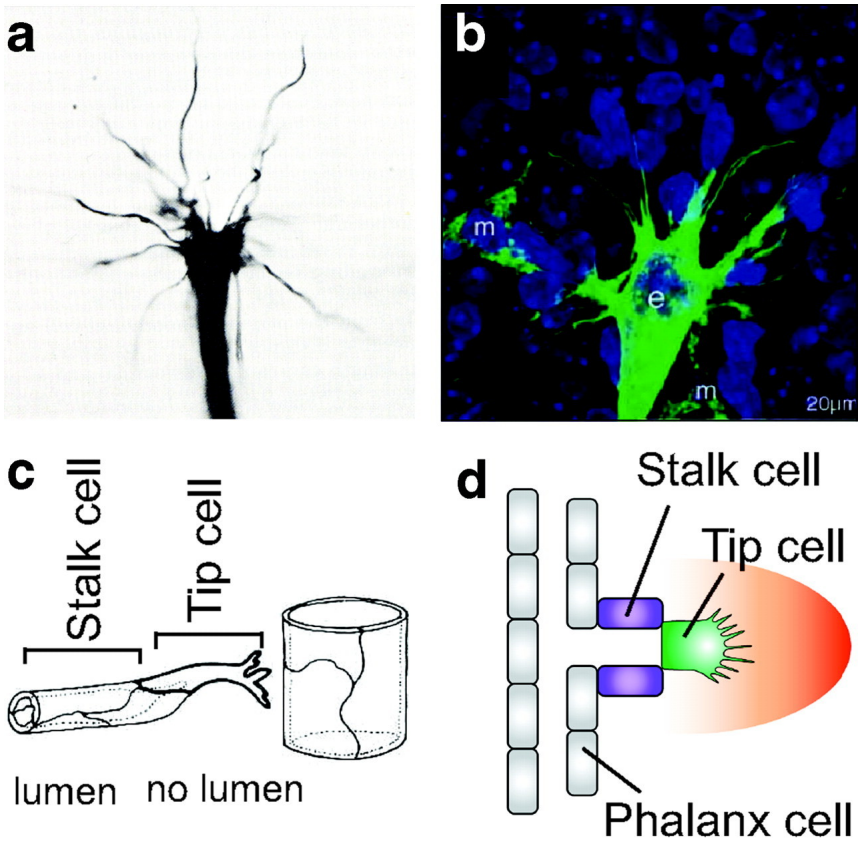

Figure 3.1: a, Original picture showing an embryonic endothelial tip cell obtained by electron microscopy. b, Confocal micrograph showing filopodia extensions at the leading tip cell. c, Scheme from 1972 proposing several endothelial subtypes in the angiogenic sprout. d, Schematic representation of a tip cell (green) extending filopodia toward an angiogenic stimulus (red gradient), followed by stalk cells (purple), while phalanx cells (gray) remain quiescent. Adapted from [31]

the number of cells increases. Continuum models are based on ordinary or partial differential equations (PDEs) that describe the blood vessels through the endothelial cell density or volume fraction that evolves in time. [29, 22, 3]. Continuum models are capable of capturing macroscopic features related to vasculature, HIF, and ECM. Meanwhile, PDEs describe movement due to diffusion, haptotaxis, and chemotaxis [40, 85]. While continuous models offer advantages such as low computing costs and the utilization of parallel solvers, they are limited in their ability to resolve local key features of the changing vasculature, including, for example, the activation of TECs and the competition for the TEC phenotype among other TECs and neighboring endothelial cells [54]. To balance both approaches and produce robust and sophisticated vascular fields, Hybrid models integrate both continuum and discrete descriptions into a single framework. In hybrid models, TECs are depicted as discrete agents migrating chemotactically following the HIF gradient and endothelial cell density are modeled using a continuum approach describing the movement, proliferation, and apoptosis. We refer the interested reader to the reviews in [33, 34, 94, 26].

Motivated by the need to better understand the complex dynamics of angiogenesis and its critical role in cancer progression, the objective of this work is to develop a hybrid mathematical model that captures the key biological processes involved. Specifically, we aim to integrate hypoxia inducible factor dynamics, capillary sprouting, tip endothelial cells and the role of specialized filopodia in guiding the formation of new vascular networks. By combining continuum and discrete modeling approaches, our hybrid framework seeks to bridge the cellular and tissue scales, enabling the resolution of capillary-level features while simulating long-term angiogenesis dynamics. In particular, we uniquely combine a focus on the filopodia as modeled by a set of check points that mimic the high concentration of receptors of TECs. Ultimately, this work aims to contribute to a mechanistic understanding of angiogenesis, which could inform the development of more effective anti-angiogenic therapies and advance our knowledge of cancer biology.

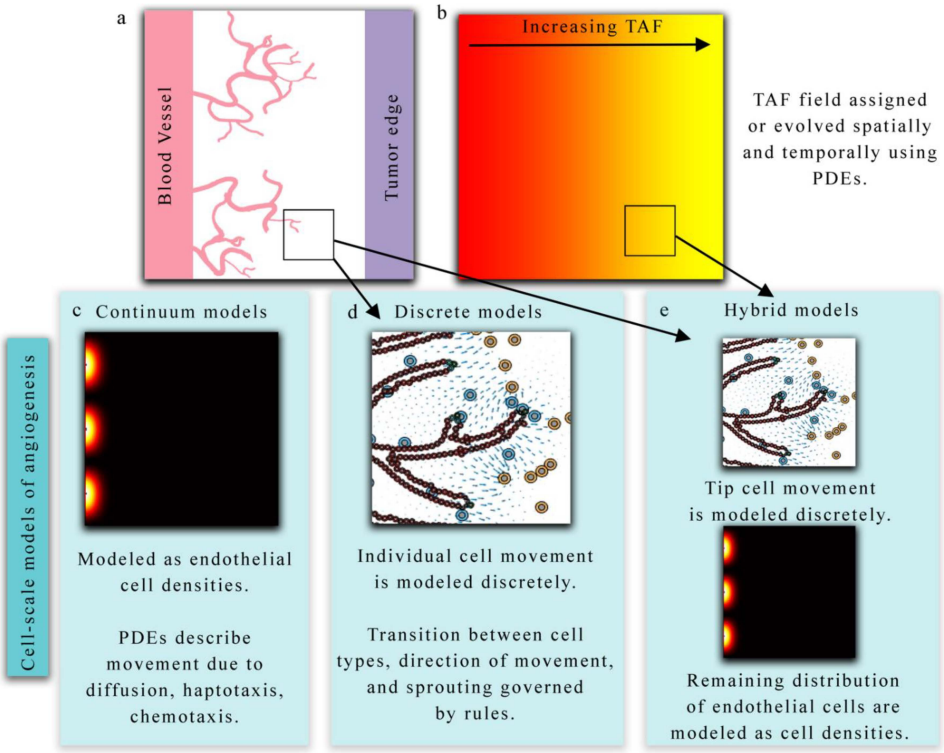

Figure 3.2: Overview of cell-scale models of angiogenesis. Adapted from [54]

3.2 Mathematical model

In this chapter, we present a multiscale model for angiogenesis growth based on the phase-field theory, developed by Vilanova et al [87, 86]. The model incorporates the dynamics of capillaries, angiogenic factors, and tip endothelial cells (TECs), along with a discrete conceptualization of filopodia that enables TECs to sense their microenvironment. Here, the new feature is that the modeling of filopodia and filopodia-influenced migration are achieved in a concise and more compatible manner. While steering clear of many potential bugs in simulations, our model preserves biological mechanisms and demonstrates a strong capability to simulate the development of angiogenesis with complex morphologies. This paves the way for our future work in Chapter.4, specifically the development of a model that integrates tumor growth and angiogenesis

3.2.1 Capillaries

Following [87], the dynamics of capillaries is modeled using the phase-field theory, which describes the evolution of a continuous variable c that represents the capillary [82]. The phase-field theory is a mathematical formalism to derive models for problems with moving interfaces. See [23, 35, 57] for reviews . In each of the phases, with a smooth change between phase values in a thin layer of finite width around the interface. Here, phase fields are used to indicate the locations of various cell types. Specifically, we employ two phase fields: one to identify the position of endothelial cells, and the other to indicate the location of hypoxic cells. The phase-field equation is derived from an energy functional that accounts for the surface and chemical free energies of the system. According to the phase-field theory, endothelial cell location is indicated by the order parameter c, which evolves in a way that tends to adopt the configuration of minimum energy provided by the energy functional

$$\varepsilon(c, f) = \int_{\Omega} (\Psi_s(c) + \Psi_c(c, f))dx, \tag{3.1}$$

where Φ_s and Φ_c are the so-called surface free energy and chemical free energy, respectively. The surface energy is defined as

$$\Psi_s(c) = \frac{1}{2}\lambda^2|\nabla c|^2, \tag{3.2}$$

where λ is a positive constant proportional to the width of the capillary wall and $|\cdot|$ denotes the magnitude of a vector. The chemical free energy is given by

$$\Psi_c(c, f) = \frac{1}{4}(c+1)^2(c-1)^2 + \frac{1}{2}\alpha\gamma(f)(c+1)^2(2-c)^2, \tag{3.3}$$

which is a double-well non-convex function with two local minimal, where α is a parameter and $\gamma(f)$ is a tilting function which defined as

$$\gamma(f) = exp[-exp(\beta(f - f_{fact}))] - exp(-1), \tag{3.4}$$

where β is an constant. Each local minimum presents a phase. At $c = 1$, the concentration of endothelial cells reaches its maximum. While $c = -1$, there are no endothelial cells, that is, extravascular tissue. The phase-field dynamic equation is

$$\frac{\partial c}{\partial t} = -M\frac{\delta \varepsilon}{\delta c} \tag{3.5}$$

$$\frac{\delta \varepsilon}{\delta c} = -\lambda^2 \Delta c + \mu(c, f) \tag{3.6}$$

$$\mu(c, f) = \frac{1}{2}(c^2 - 1)(c - 3\alpha\gamma(f)) \tag{3.7}$$

where M is the mobility, $\frac{\delta \varepsilon}{\delta c}$ is the variational derivative of the energy ε, and $\mu(c, f)$ is the derivative of the Ψ_c with respect to the order parameter. Gathering Eq. 3.5 - 3.6, we have the following reaction–diffusion partial differential equation for capillary c:

$$\frac{\partial c}{\partial t} = M(\lambda^2 \delta c - \mu(c, f)). \tag{3.8}$$

3.2.2 Hypoxia inducible factor (Angiogenic factor)

The angiogenesis generates a vascular network based on pro-and anti-angiogenic factors. Some of these substances promote angiogenesis, such as VEGF or bFGF, while others in some way hinder the development of new sprouts, such as TSP-1 or Ang-2. As a consequence, hypoxic cells are ultimately able to draw endothelial cells from their tightly controlled homeostatic condition through the unbalancing of the angiogenic factor equilibrium towards angiogenesis [61]. Let f represents the net pro-angiogenic contribution of all these sub-

stances. We assume that the net angiogenic factor (NAF) secreted by hypoxic cells (HYCs) diffuses throughout the tissue, decays naturally, consumed by endothelial cells, forming well defined spatial concentration gradients, and eventually triggers angiogenesis.

Hypoxic cells (HYCs) are modeled here as circular, mesh-free, discrete agents with a radius R. These cells continuously release the HIF unless they receive sufficient nutrients, signifying the presence of a capillary in close proximity to them ($c > 0.9$).

The dynamics of f is supposed to be governed by the reaction-diffusion equation

$$\frac{\partial f}{\partial t} = \nabla \cdot (D \nabla f) + \mathcal{P}(d)(f_{hyc-f}) - \mathcal{U}(c) f, \tag{3.9}$$

where D is the diffusion coefficient and f_{hyc} is a constant representing the maximum NAF concentration in the tissue. $\mathcal{P}$ is defined as

$$\mathcal{P} = \begin{cases} P & \text{if } d < R \\ 0 & \text{if } d \geq R. \end{cases} \tag{3.10}$$

Here, P is the production rate, d is the distance to the closest hypoxic cells and R is an average cell radius. The uptake function $\mathcal{U}$ is defined as

$$\mathcal{U} = \begin{cases} U_u c & \text{if } c > 0 \\ -U_d c & \text{if } c < 0, \end{cases} \tag{3.11}$$

where U_u is the endothelial cell uptake rate, and U_d combines the AF decay rate and the uptake rate by other cells.

3.2.3 Tip endothelial cells

Sprouting angiogenesis is led by TECs, which specialized cells at the extremity of newly formed capillaries that extend filopodia and guide capillary outgrowth [32]. Key features of TECs are their location at the forefront of vessel branches, highly polarized nature, and numerous filopodia probing the environment, while migrating toward an angiogenic stimulus, such as the direction of increasing VEGF concentration [31].

When capillaries receive NAF signals, some privileged cells (TECs) acquire a migratory phenotype and lead the growth of new sprouts. When an endothelial cell becomes a TEC, it expresses Delta-like ligand 4 (Dll-4) [81]. Expression of the Notch ligand Delta-like-4 (Dll4) in TECs suppresses tip cell fate in neighboring stalk cells via Notch signaling. This factor is overexpressed by TECs and binds to the Notch receptors of nearby endothelial cells, preventing the adjacent cells from becoming TECs and thereby optimizing the number of TECs [30, 50]. For supporting experimental evidence, we referred to [52, 42, 51].

The key job of TECs is to navigate, a process that relies on correct probing of microenvironmental cues, and translating them into a dynamic process of adhesion (at the front) and deadhesion (at the rear), that ultimately leads to cell movement. To navigate, tip cells become polarized and leading front extends filopodia, whereas their rear maintains contact with trailing stalk cells to avoid branch desintegration [31]. Filopodia are able to sense their microenvironment and increase the chemical sensitivity of TECs, facilitate their migration following chemotactic cues and permit tip endothelial cells to detect nearby capillaries [10]. For these reasons, tip endothelial cells are modeled here as circular (with radius R), mesh-free, discrete agents that can get activated and deactivated, spread filopodia, move following chemotactic gradients of tumor angiogenic factor, detect nearby capillaries, and anastomose with them [92].

Here, we show the details about deterministic rules as follow:

- **Activation**

  To active a new tip endothelial cell, the following conditions must be met:

  1. $c \geq c_{act}$ which guarantees that the point is inside a capillary;
  2. $f > f_{act}$ the concentration of NAF is greater than a certain threshold;
  3. $||x - x_{TEC}|| > \delta_4$ the distance to any other tip endothelial cell is larger than δ_4 which represents the diffusion length of the ligand Dll-4.

By preventing TECs to be formed in the surroundings of another active tip cell, we encode the essential mechanism whereby Dll4 controls the density of the vascular network. Note that whenever there are several points satisfying all the conditions listed above, we randomly choose one for each iteration.

- **Filopodia**

  We implement the filopodia around each tip cell (which mimics high concentration of receptors) as a set of check points that capable of detect nearby vessels.

  1. The filopodia check points are evenly positioned on the edge of an sector.
  2. The angle of sector is $\theta = \frac{2\pi}{3}$, centered around the chemotactic direction.
  3. The radii of the sector is set to $\mathcal{L} = 4R$, where R is the radius of TECs.

  In [87], Vilanova et al. model filopodia as an annular sector but with 2 layers. The internal and external radii of the annular sector are set to $\mathcal{L}_{ext} = 2R$ and $\mathcal{L}_{ext} = 4R$, representing Lamellipodia and Filopodia, respectively. The role of external layer filopodia is to detect a capillary and leading the the direction of migration. The role of internal layer is to model anastomosis by testing whether the value of c. Different with [87], We only utilize the edge of a sector, which consists of only one external layer, to mimic the filopodia and implement direction guidance and anastomosis. The reasons for doing this will be discussed after presenting the model.

- **Migration**

  Activated TECs have two types of migration scenarios:

  1. Activated cells migrate through the extracellular matrix following chemotactic cues with a velocity proportional to the gradient of net pro-angiogenesis factor(NAF), given by

  $$v = \chi \frac{\nabla f}{|\nabla f|}, \tag{3.12}$$

  where χ is the chemotactic constant and $|\cdot|$ denotes the Euclidean norm.

  2. When any of the filopodia checkpoints detects a nearby capillary or basement membrane, filopodia adhere and form focal contact points to connect the cytoskeleton to the extracellular matrix (ECM). This allows stress fibers of actin/myosin filaments to pull the TEC toward these anchors, and induce forward movement [31]. In our model, we record the adhesion points as the destination of the TECs. the moving direction of the TEC changes towards the adhesion point and the speed is maintained.

- **Deactivation**

  When one of the following condition is met, TEC become deactivated and loses its migratory phenotype:

  1. TEC anastomoses with capillary. When the TEC move to the adhesion point that identified by the filopodia checkpoint, indicating that the TEC is in contact with the capillary, an anastomosis event occurs, leading to the deactivation of the TEC.

  2. $f < f_{act}$ When the NAF is scarce, the stimulus ceases, and the TEC become deactivated.

In [87], Vilanova et al. provide a complex filopodia model that attempts to closely follow biological mechanisms and work in most case (See Fig. 3.3). However, they set the annular sector centered around the chemotactic direction, and the annular sector direction remains unchanged after the filopodia detect a capillary. This setting not only fails to conforms to the biological mechanism but also introduces unnecessary bugs in the simulations. When the filopodia-influenced migration brings a TEC close to the capillary, the annular sector direction deviates from the the direction of movement and the degree of deviation depends on the concentration difference of HIF.

For example, in Fig. 3.3, the concentration of HIF(f) around the capillary is much lower than elsewhere due to its consumption by the capillary. Thus, when a TEC migrate close to a capillary, the direction of its annular sector undergoes severe deviations due to a strong change in the gradient of HIF. In simulations, it consistently occurs that capillaries cannot be detected by the inner layer, or the inner layer detects its own stalk, leading to the overgrowth of tip endothelial cells (TECs) or sudden stops, which are beyond expectations.

Surprisingly, relatively little is known about the processes regulating the assembly of these cellular protrusions in ECs, which gives us more possibilities to improve this model. Here, in Fig. 3.4, our model successfully addresses the problem in a concise and more compatible way by using only the external layer to achieve detection and anastomosis. This improvement avoids potential unexpected occurrences while preserving its biological mechanisms.

From a technical perspective, the fundamental challenge in developing hybrid model is the need to bridge the cellular and tissue scales and couple the continuous variables and discrete agents. In our work, the connection between these two parts of the model is that both the TECs and the continuous variable c describe endothelial cells. Thus, we include TECs in the phase-field variable using a straightforward approach: c is updated to $c = 1$ in those regions of the computational domain occupied by TECs. We use smoothed-out radial Heaviside functions which take approximately the value $+1$ inside the circular cell and -1 elsewhere

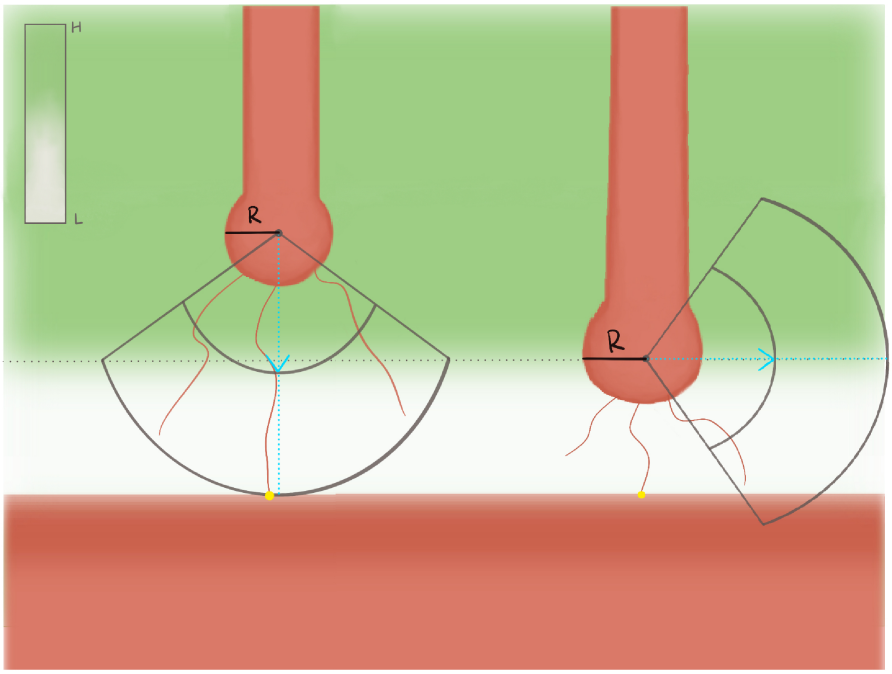

Figure 3.3: The model of filopodia described in [87].

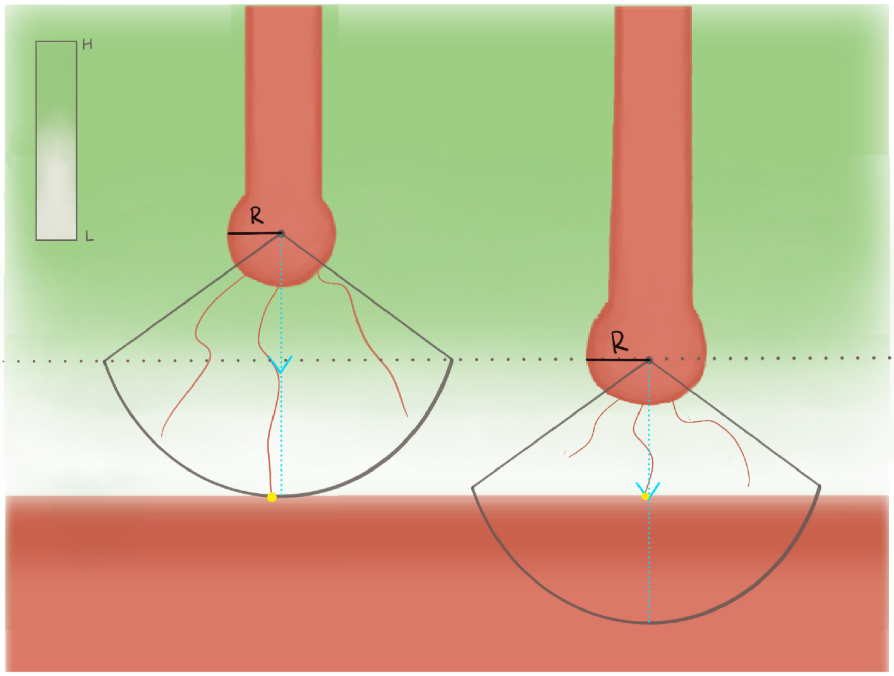

Figure 3.4: The model of filopodia described in our model.

as template function. Then we define simple approximations to a phase field representing a single circular cell and use that as a template which moves following TECs.

3.3 Numerical results

3.3.1 Two main vessels

We start with a simulation to study the development of angionenesis from a pre-existing vessel network with simple domain. We perform the simulation on a square domain, $\Omega = (0, 300) \times (0, 300)$ using a uniform mesh 256×256. The boundary conditions are zero-flux conditions. The initial setup of the simulation shown in Fig. 3.5, we set up two straight capillaries along the opposite edges of the square domain(top and bottom). In the central region, we set an cluster of hypoxic cells within a tumor-like circular area that continuously release HIF. 150 hypoxic cells with average cell radius R are randomly distributed in the region which is equidistant to the top and bottom boundaries.

The simulation time $T = 20$ and the time step $dt = 5 \times 10^{-4}$. The parameter values in dimensionless units used in the computations are summarized in Table.3.1. The computational simulation involves a finite difference scheme in a MATLAB script.

Fig. 3.6 shows the time evolution of the simulation. At $t = 1$, we observe that two TECs get activated on both sides and initially migration following the chemotactic direction. In the second snapshot, several time steps afterwards, two other TECs get activated from the top and grow parallel to each other separated by a distance. One new TEC get activated from the new capillary on the bottom which create the first branch. At $t = 4$, the network starts to create more branches and bifurcation. Moreover, at $t = 5, 6$, as more capillaries grow behind and branching, the distance between TECs and capillaries falls within the extension

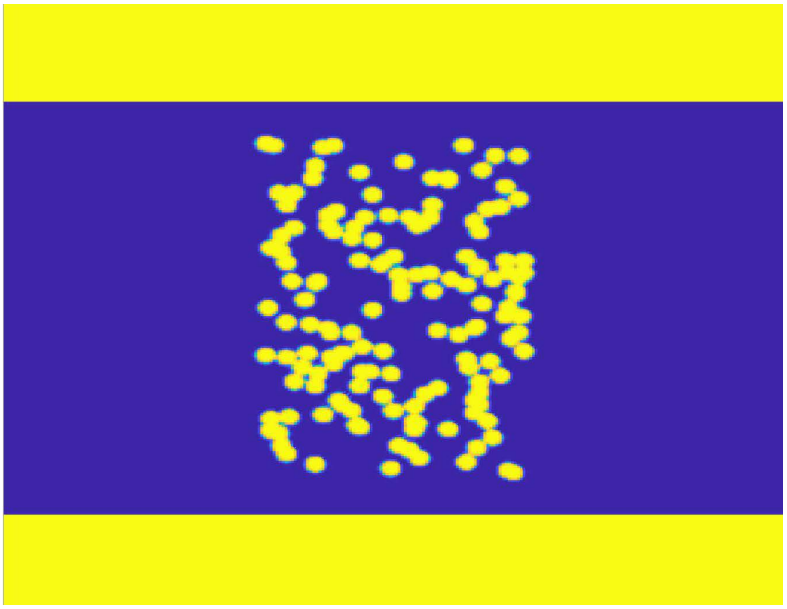

Figure 3.5: The initial setup of the angiogenesis model.

range of filopodia, which triggers the creation of anastomoses.

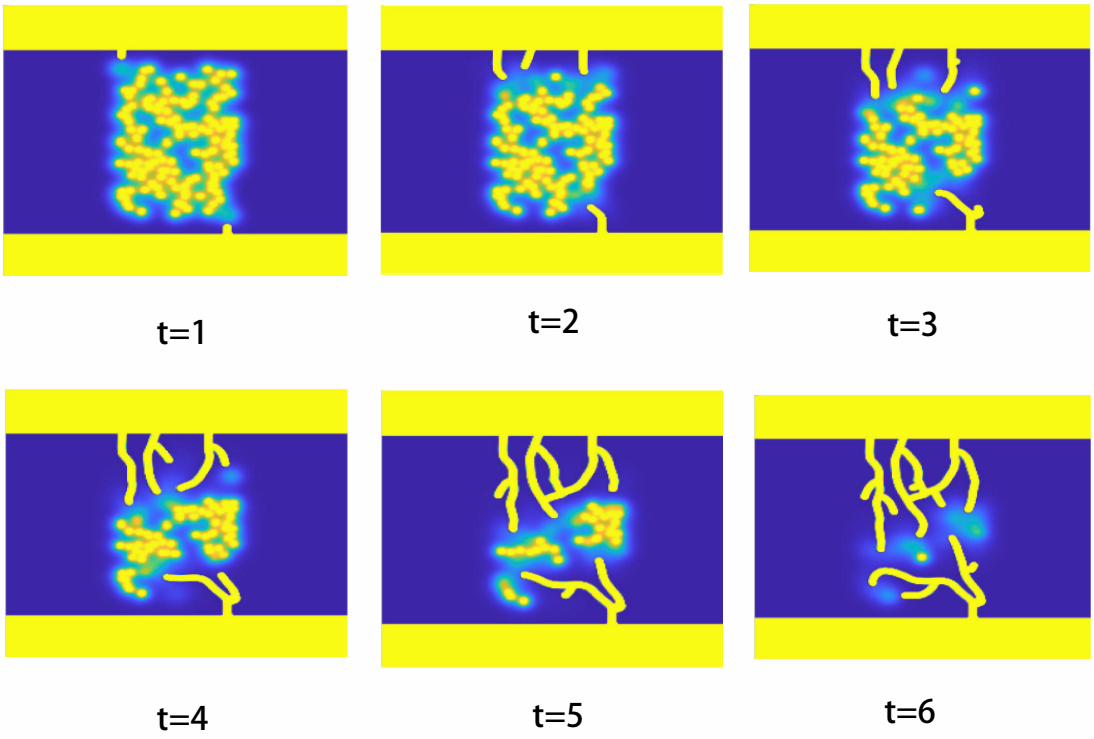

Figure 3.6: Evolution of the formation of angiogenesis.

Table 3.1: Parameters of the angiogenesis model in dimensionless units.

parameter	description	value
D	tumor angiogenic factor diffusion coefficient	300.0
f_{hyc}	maximum tumor angiogenic factor concentration in the tissue	1.0
P	tumor angiogenic factor production by HYCs	350
R	average cell radius	4.0
U_u	tumor angiogenic factor endothelial cell uptake	60.875
U_d	tumor angiogenic factor natural decay	15.35
λ	interface width	1.0
M	mobility	0.0975
χ	chemotatic constant of tip endothelial cells	250.47
c_{act}	condition for TEC activation	0.9
f_{act}	condition for TEC activation	0.01
δ_4	Dll-4 radius of action	28
δ_{nox}	condition for HYC deactivation	10

3.4 Discussion

In this chapter, we proposed a multiscale model for angiogenesis growth. The model is composed of two continuum variables and a set of discrete agents. The dynamics of capillaries is modelled using the phase field theory at full scale to simulate long-term dynamics of angiogenesis. The pro-angiogenic fact diffuse form the hypoxic cells and the dynamics is governed by the reaction-diffusion equation. Tip endithelial cells are discrete agents in our model. Simultaneously, we have included a discrete conceptualization of filopodia that endows TECs with the ability to sense their microenvironment. The setup for filopodia is simple, compatible, and aligns with biological mechanism, laying the groundwork for its seamless integration with future tumor-induced angiogenesis models.

Chapter 4

Mathematical Modeling of Tumor Angiogenesis

4.1 Introduction

Tumor angiogenesis is intricate, a multiple-step process which resulting in the development of solid malignancies. The observation that angiogenesis occurs around tumors was made nearly 100 years ago, and the hypothesis that tumors produce a diffusible angiogenic substance was put forward in 1968 [21]. Due to its prominent role in cancer metastasis, tumor angiogenesis is one of the major areas of cancer research in recent years [74, 56].

Angiogenesis is the formation of new blood vessels from the endothelial cells (ECs) of pre-existing veins, arteries, and capillaries. The growth process is usually triggered by cells whose oxygen or nutrient requirements are not satisfied by the current vasculature and it can happen both in physiological and pathological conditions [87]. In normal tissues, angiogenesis is carefully self-regulated and tightly controlled. However, in cancer, the vessels are structurally and functionally abnormal. In the avascular stage of tumor growth, a significant amount of

nutrients is consumed due to rapid proliferation of tumor cells. Inefficient nutrient delivery to tumor cells results in regions of severe hypoxia that hinders tumor growth. This is a trait observed in nearly all solid malignancies [84]. To overcome the oxygen-deficient microenvironment, hypoxic tumor cells secrete tumor angiogenesis factor (TAFs), such as vascular endothelial growth factor (VEGF, [53]), or basic fibroblast growth factor (bFGF, [7]) which unbalance the equilibrium between pro- and anti-angiogenic substances and trigger the formation of new blood vessels [56, 14]. TAFs diffuse outward from the hypoxic regions of the tumor and eventually reach the neighboring blood vessels.

Blood vessels are lined by endothelial cells (ECs) and the growth of new sprouts requires these cells to migrate and proliferate [58]. After being detected by ECs, TAFs secrete matrix degrading enzymes that are able to break down the basement membrane and the extracellular matrix (ECM). ECs begin to migrate from the original blood vessel towards the tumor. Under the influence of TAFs , endothelial cells(ECs) differentiate into two phenotypes. The first migrating ECs are termed tip endothelial cells (TECs) which can sense their environment and direct the sprouting process. To establish a properly patterned vascular tree, TECs must be followed by morphologically distinct EC, which form a lumenized tube growing behind the TEC. In contrast to the tip cells, these follower cells termed stalk endothelial cells (SECs) that exhibit proliferative behavior.

Furthermore, during angiogenesis, VEGF and Notch signaling pathways are involved in the differentiation of TECs and SECs in the vascular endothelium. Under the stimulation of VEGF, the expression of Delta-like ligand 4 (Dll4) is up-regulated in TECs. Dll4 binds to Notch receptors of nearby endothelial cells which, in turn, reduces their VEGF receptor expression, consequently suppressing their TEC phenotype. See [13, 50] for more details.

Experimental evidence shows that vessels grow led by TECs. TECs migrate mainly following the gradient of tumor-produced growth factors and also facilitated by filopodia [51]. Filopodia are rod-like cell surface projections filled with bundles of parallel actin filaments

that function as antennae for TECs to probe their microenvironment [64, 37]. In particular, when filopodia sense the remnants of basement membrane, TECs alter their direction towards them, using them as the path of minimum resistance in their migration. Then, the vessels link with the old ones and form a network of loops during a process called *anastomosis*. The resulting neovasculature provides the tumor with a direct supply of oxygen and other nutrients. Nourished by this new vascular network, cancer cells begin a stage of rapid proliferation.

Tumor growth is a complex process that involves the interplay of various cell types, including cancer stem cells (CSCs), differentiated cancer cells, and dead cells [49]. Mathematical models of tumor growth can capture the dynamics of these cell populations, their interactions with the microenvironment, and the influence of nutrients and signaling factors on tumor progression[62]. In a general tumor growth model, tumor cells can proliferate, differentiate, and die. They can also switch phenotypes depending on the local microenvironment and signaling cues [44, 98]. Moreover, tumor cells can adapt their metabolic preferences depending on the oxygen levels in their surroundings. In well-oxygenated regions, cells may prefer oxidative phosphorylation (OXPHOS) for energy production, while in hypoxic areas, they may switch to glycolysis, which is less efficient but does not require oxygen. Another crucial aspect of tumor growth is the production of angiogenic factors by tumor cells[39, 11]. These factors, such as vascular endothelial growth factor (VEGF), stimulate the formation of new blood vessels (angiogenesis) to supply the growing tumor with oxygen and nutrients. Different tumor cell types may produce angiogenic factors at varying rates, depending on their phenotype and the local oxygen concentration [72, 95]. For example, hypoxic cells may secrete higher levels of angiogenic factors compared to well-oxygenated cells, as a response to the lack of oxygen.

By coupling tumor growth models with angiogenesis model, we can gain a more comprehensive understanding of the intricate relationship between vascular development and tu-

mor expansion, which is essential for developing effective anti-cancer therapies. The tumor growth model presented in this work incorporates these key features, including cell proliferation, differentiation, death, phenotypic switching, metabolic adaptation, and angiogenic factor production, to provide a detailed representation of the complex dynamics of tumor progression."

Motivated by the need to better understand the complex dynamics of tumor-induced angiogenesis and its critical role in cancer progression, the objective of this work is to develop a comprehensive mathematical model that captures the key biological processes involved. Specifically, we aim to integrate the distinct yet interconnected mechanisms of tumor growth, angiogenic factor dynamics, capillary sprouting, and the role of specialized endothelial cells (tip cells) in guiding the formation of new vascular networks. By coupling tumor growth models with angiogenesis models, our hybrid framework seeks to bridge the cellular and tissue scales, enabling the resolution of capillary-level features while simulating long-term angiogenesis dynamics. Furthermore, by incorporating experimental data from the novel vascularized microtumor (VMT) platform, we strive to validate our model against realistic vascular morphologies and gain insights into the intricate interplay between tumor cells, angiogenic factors, and the evolving vasculature. Ultimately, this work aims to contribute to a mechanistic understanding of tumor-induced angiogenesis, which could inform the development of more effective anti-angiogenic therapies and advance our knowledge of cancer biology.

4.2 Extraction of the initial vasculature network from VMT device images

The vascularized microtumor (VMT) platform, developed by [46], is a novel in vitro system that recapitulates the complex tumor microenvironment, including a perfused vascular network, within a microfluidic device. The VMT platform allows for the co-culture of tumor cells and endothelial cells in a three-dimensional extracellular matrix, enabling the formation of a vascularized microtumor that closely mimics the in vivo tumor microenvironment. As an example, a fluorescent image of VMT with a fully-developed vascular network is shown in Fig. 4.1.

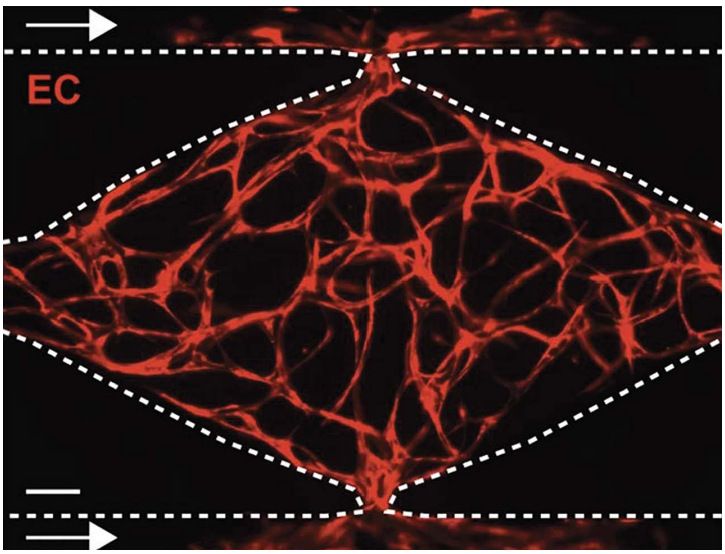

Figure 4.1: Fluorescent image of tissue chamber with a fully-developed vascular network. Vessels in red. Adapted from [78]

The VMT device consists of a central chamber for co-culturing tumor cells and endothelial cells, surrounded by microfluidic channels that allow for the perfusion of the vascular network. The central chamber of the VMT device is filled with a three-dimensional extracellular matrix, such as collagen or fibrin, which provides a supportive scaffold for the growth

and organization of the tumor cells and endothelial cells. The composition and stiffness of the extracellular matrix can be tailored to mimic the specific tumor microenvironment of interest. Tumor cells and endothelial cells are seeded into the central chamber of the VMT device, where they self-organize and form a vascularized microtumor. The endothelial cells form a perfusable vascular network that supplies the tumor cells with oxygen and nutrients, recapitulating the critical role of angiogenesis in tumor growth and progression. The vascular network within the VMT device is perfused with cell culture media or allowing for the study of tumor-vasculature interactions under physiologically relevant flow conditions. The optically transparent nature of the device enables real-time, high-resolution imaging of the vascularized microtumor using fluorescent microscopy, confocal microscopy, or light sheet microscopy.

The VMT platform recreates the complex tumor microenvironment, including a perfused vascular network, which more closely resembles the in vivo situation compared to traditional 2D cell culture or avascular 3D models.

In the context of our hybrid model of tumor angiogenesis, the VMT platform serves as a valuable source of experimental data for initializing and validating our simulations. By extracting the initial vascular network from fluorescent images of the VMT device and incorporating it into our model, we can simulate tumor-induced angiogenesis in a biologically relevant context and compare our results with the observed vascular morphologies in the VMT platform. This integration of experimental data and computational modeling provides a powerful approach for understanding the complex dynamics of tumor angiogenesis and identifying potential therapeutic targets. We refer to [78, 70, 45, 46] for more details about VMT platform.

4.3 Mathematical model of tumor induced- angiogenesis

4.3.1 Angiogenesis model

The angiogenesis model is developed and described in Chapter 3, which incorporates the dynamics of capillaries, angiogenic factors, and tip endothelial cells (TECs), along with a discrete conceptualization of filopodia. The dynamics of capillaries are modeled using a continuum approach describing the movement, proliferation, and apoptosis of the cells within the capillaries. Reaction-diffusion equations are used to describe the dynamics of chemical substances (VEGF). Meanwhile, the model of tumor and capillary growth is based in a phase-field theory that allows one to resolve capillaries at full time case and to simulate long-term dynamics of angiogenesis. TECs are identified within the field of capillaries based on the concentration of TAF and lateral inhibition (no TECs are within a distance threshold of the cell to be activated). Furthermore, a discrete conceptualization of filopodia has been incorporated, granting TECs the ability to sense their microenvironment. See chapter.3 for more details.

4.3.2 Tumor growth model

The tumor growth model presented in this work is based on a diffuse interface continuum model of multispecies tumor growth that considers the dynamics of cancer stem cells (CSCs), differentiated cancer cells (Wnt-Hi and Wnt-Mod), and dead cells. The model incorporates the effects of nutrients (oxygen and glucose), signaling factors (Wnt, DKK4, FGF, FGF20 and BMP), and lactate on tumor cell proliferation, differentiation, and death. The model is well-posed and consists of fourth-order nonlinear advection–reaction–diffusion equations

(of Cahn–Hilliard-type) for the cell species. The self-renewal probabilities of CSCs and differentiated cancer cells are regulated by the concentrations of Wnt, FGF, and BMP, which are modeled using reaction-diffusion equations. The proliferation rates of tumor cells depend on the availability of oxygen, glucose, and lactate, as well as the influence of signaling factors. The schematic of the model is shown in Fig. 4.2

Tumor cells are modeled as volume fractions. The governing equations for each cell type are derived from mass conservation equations that account for cell motility, proliferation, apoptosis, and switching among cell types. Signaling pathways identified by the scRNAseq analysis are modeled as spatiotemporally varying signaling factors that feedback on the proliferation rates and self-renewal fractions of tumor cells.

The model is illustrated in Fig. 4.2. The tumor consists of cancer stem cells (CSC), Wnt-Hi, and Wnt-Mod cells characterized by different levels of Wnt signaling, as well as dead cells (not shown in the diagram). CSC have three possible outcomes when they divide: (1) CSC may self-renew in regions with low levels of Wnt signaling, or (2) switch to Wnt-Hi cells in regions with high Wnt signaling, or (3) switch to Wnt-Mod cells in regions with moderate Wnt signaling. Similarly, Wnt-Hi and Wnt-Mod cells may self-renew at high or moderate levels of Wnt signaling, respectively. They may also switch to other cell types, indicated by the double arrows. We assume the tumor produces a factor F that belongs to the FGF superfamily and signals through FGFR4 or FGFR3 to CSC. This factor is released by CSC (and non-CSC at a much lower rate) and is essential for the proliferation and self-renewal of CSC. Wnt-Hi and Wnt-Mod cells may switch to CSC when the factor F is present.

Wnt-Hi cells (together with other tumor cells at a lower rate) release Wnt as a short-range activator, as well as its long-range inhibitor Dkk. The Wnt-Dkk system is responsible for pattern formation [25]. When the Wnt level is low, tumor cells are oxidative. Cell proliferation requires oxygen, and cells may consume glucose or lactate. When Wnt is high, the tumor switches to glycolysis, in which the cells consume glucose to proliferate. The proliferation

rate is regulated by positive feedback factors (e.g., FGF) and negative feedback factors (e.g., BMP), both are released by all tumor cells, as indicated by the cell to cell communications in Figure 2A. The stroma also releases FGF and Wnt that freely diffuses into the tumor. See the Table.4.2 for model parameters. The complete model are described as follows.

Wnt signaling is necessary for tissue development and homeostasis, but aberrant, overactive signaling is present in almost half of known human cancers [97, 24, 12]. Colorectal cancer is the signature tumor type where chronically high Wnt signaling causes more than $80-90\%$ of cases. The mechanism by which Wnt signaling is overactivated is well understood: genetic mutations that inactivate at least one component of a cytoplasmic "destruction complex" for the mediator β-catenin lead to its Wnt-ligand-independent translocation and accumulation in the nucleus where it is recruited by TCF/LEF transcription factors for upregulation of Wnt target genes It is the upregulation/dysregulation of targets that triggers cell transformation, and it is assumed that every subsequent cancer cell with this mutation carries aberrantly high levels of nuclear β-catenin and expression of target genes. Despite knowing these basics for almost 20 years, there are no Wnt inhibitors in the clinic. A great deal of the problem rests with the issue that biomarkers of active Wnt signaling (i.e. nuclear localized β-catenin and target gene expression), are heterogeneous in human tumors [17, 16]). Most studies have focused on the influence of the tumor microenvironment, noting that beta-catenin is upregulated in cells near invading edges [17, 16]. But aside from making assumptions that cancer associated fibroblasts signal to upregulate beta-catenin and that these cells are the invasive portion of the tumor, there has been little progress in testing these assumptions. Clearly, there is a need to better understand Wnt heterogeneity so that we have can better target Wnt signaling in cancer.

Following previous studies of the three-dimensional multispecies mixture model [96, 93], we present the complete set of equations for the tumor growth model. We assume the cells are tightly packed, and cell species are modeled as volume fractions. Let φ_0, φ_1, φ_2, and φ_D are

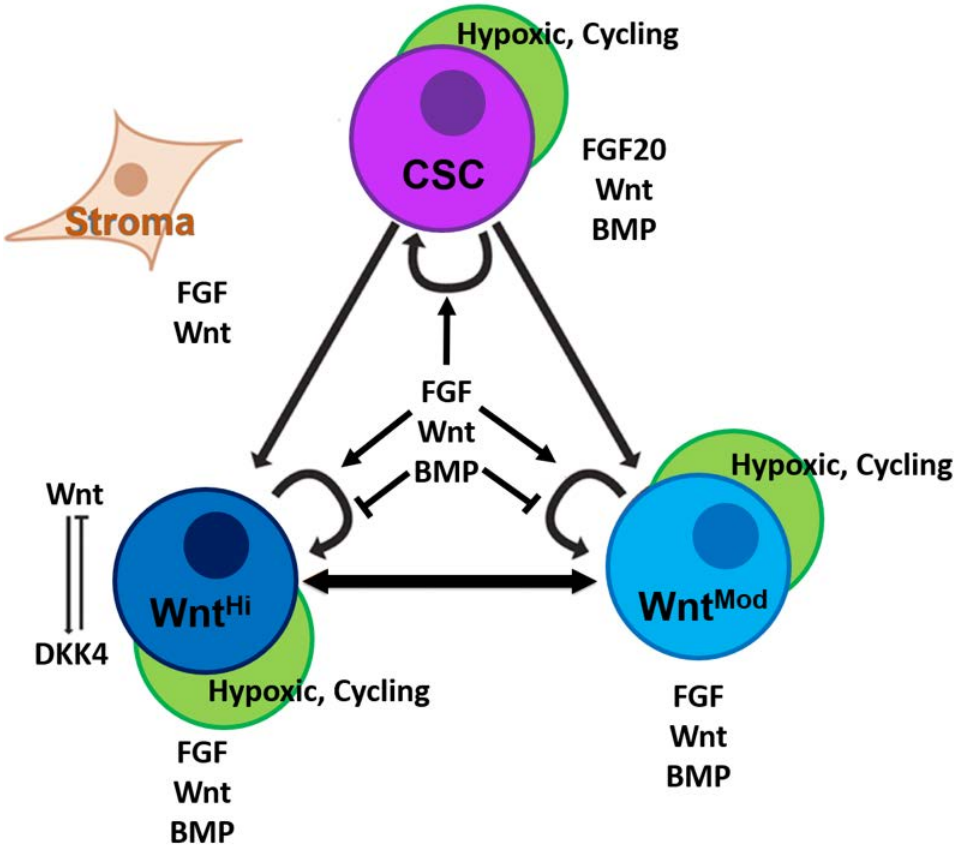

Figure 4.2: Schematic of the tumor growth model.

the volume fraction of CSC, Wnt-Hi, Wnt-Mod, and dead cells, respectively. The volume fraction of total tumor cells is $\varphi_T = \varphi_0 + \varphi_1 + \varphi_2 + \varphi_D$.

The volume fraction of total tumor cells (φ_T) satisfies the mass conservation (advection-reaction-diffusion) equation:

$$\frac{\partial \varphi_T}{\partial t} + \nabla \cdot (u_s \varphi_T) = \nabla \cdot (M \varphi_T \nabla \mu) + Src_T, \tag{4.1}$$

$$Src_T = \lambda_{m0}\varphi_0 + \lambda_{m1}\varphi_1 + \lambda_{m2}\varphi_2 - \lambda_L \varphi_D \tag{4.2}$$

where M is the cell mobility, Src_T is the mass-exchange term of total tumor cells, λ_L is the lysis rate of dead cells. We introduce the chemical potential μ and adhesion energy E:

$$\mu = \frac{\delta E}{\delta \varphi_T}, \tag{4.3}$$

$$E = \frac{\gamma}{\varepsilon} \int_\Omega f(\varphi_T) + \varepsilon^2 |\nabla \varphi_T|^2 \, dx, \tag{4.4}$$

where γ measures cell to cell adhesion, ε is the thickness of cancer-host interface, $f(\varphi_T) = \frac{1}{4}{\varphi_T}^2 (1 - \varphi_T)^2$ is a double-well potential that penalizes mixing of the cancer cells. $\frac{\delta E}{\delta \varphi_T}$ is variational derivatives of the adhesion energy:

$$\frac{\delta E}{\delta \varphi_T} = \frac{\gamma}{\varepsilon}(f'(\varphi_T) - \varepsilon^2 \nabla^2 \varphi_T), \tag{4.5}$$

Mass-averaged velocity of solid components u_s defined by Darcy's law

$$u_s = -(\nabla p - \mu \nabla \varphi_T), \tag{4.6}$$

where p is the solid pressure:

$$-\nabla^2 p = Src_T - \nabla \cdot (\frac{\delta E}{\delta \varphi_T} \nabla \varphi_T). \tag{4.7}$$

We also model the advection of cell substrates with the interstitial liquid velocity u_w by Darcy's law:

$$u_w = -\nabla q \tag{4.8}$$

where q is the water pressure and satisfies

$$-\nabla^2 q = -Src_T. \tag{4.9}$$

4.3.3 Tumor cell species and lineage relationships

Following previous studies [40, 93], we assume Cell species and substrates in the schematic from Fig. 4.2 are solved by the equations below:

The volume fractions of CSC cells (φ_0) , Wnt-Hi (φ_1) and Wnt-Mod (φ_2): obey the mass conservation (advection-reaction-diffusion) equations that shown below with their source terms.

1. CSC(φ_0):

$$\frac{\partial \varphi_0}{\partial t} + \nabla \cdot (u_0 \varphi_0) = \nabla \cdot (M \varphi_0 \nabla \mu) + Src_0, \tag{4.10}$$

The mass exchange terms for φ_0 is

$$\begin{aligned} Src_0 = {} & (2P_0 - 1)\lambda_{m0}\varphi_0 + 2\,(1 - P_1)\,(1 - q_1)\,\frac{\chi_{10} C_{F0}}{1 + \chi_{10} C_{F0}}\lambda_{m1}\varphi_1 \\ & + 2\,(1 - P_2)\,(1 - q_2)\,\frac{\chi_{20} C_{F0}}{1 + \chi_{20} C_{F0}}\lambda_{m2}\varphi_2 \; - \lambda_{n0} H\,(\widetilde{n}_0 - n)\,\varphi_0. \end{aligned} \tag{4.11}$$

Here, λ_{m0}, λ_{m1}, and λ_{m2} are the mitosis rate of CSC, Wnt-Hi, and Wnt-Mod, respectively. λ_{n0} is the necrosis rate of CSC. $H(x)$ is the Heaviside function ($H(x) = 1$ when $x > 0$;

$H(x) = 0$ otherwise). $\widetilde{n_0}$ is the nutrient threshold of necrosis of CSC. χ_{10} is the positive feedback gain from FGF20 (C_{F0}) on the switching rate from Wnt-Hi to CSC. χ_{20} is the feedback gain on the switching rate from Wnt-Mod. See Eqns. (4-7) for the definition of switching terms P_1, P_2, q_1, q_2.

2. Wnt-Hi (φ_1):

$$\begin{aligned}
&\frac{\partial \varphi_1}{\partial t} + \nabla \cdot (u_s \varphi_1) = \nabla \cdot (M \varphi_1 \nabla \mu) + Src_1 \\
&Src_1 = (2P_1 - 1)\,\lambda_{m1}\varphi_1 + 2\,(1 - P_0)\,q_0 \lambda_{m0}\varphi_0 \\
&\qquad + 2\,(1 - P_2)\left(1 - (1 - q_2)\,\frac{\chi_{20} C_{F0}}{1 + \chi_{20} C_{F0}}\right)\lambda_{m2}\varphi_2 - \lambda_{n1} H\,(\widetilde{n_1} - n)\,\varphi_1,
\end{aligned} \tag{4.12}$$

3. Wnt-Mod (ϕ_2):

$$\begin{aligned}
&\frac{\partial \varphi_2}{\partial t} + \nabla \cdot (u_s \varphi_2) = \nabla \cdot (M \varphi_2 \nabla \mu) + Src_2 \\
&Src_2 = (2P_2 - 1)\,\lambda_{m2}\varphi_2 + 2\,(1 - P_0)\,(1 - q_0)\,\lambda_{m0}\varphi_0 \\
&\qquad + 2\,(1 - P_1)\left(1 - (1 - q_1)\,\frac{\chi_{10} C_{F0}}{1 + \chi_{10} C_{F0}}\right)\lambda_{m1}\varphi_1 - \lambda_{n2} H\,(\widetilde{n_2} - n)\,\varphi_2,
\end{aligned} \tag{4.13}$$

where λ_{n1} and λ_{n2} are the necrosis rate of Wnt-Hi and Wnt-Mod, respectively. $\widetilde{n_1}$ and $\widetilde{n_2}$ are the nutrient threshold of necrosis of Wnt-Hi and Wnt-Mod, respectively.

4. Dead cells (φ_D):

$$\begin{aligned}
&\frac{\partial \varphi_D}{\partial t} + \nabla \cdot (u_s \varphi_D) = \nabla \cdot (M \varphi_D \nabla \mu) + Src_D \\
&Src_D = \lambda_{n0} H\,(\widetilde{n_0} - n)\,\varphi_0 + \lambda_{n1} H\,(\widetilde{n_1} - n)\,\varphi_1 + \lambda_{n2} H\,(\widetilde{n_2} - n)\,\varphi_2 - \lambda_L \phi_D,
\end{aligned} \tag{4.14}$$

where λ_L is the lysis rate of dead cells.

We assume that tumor cell proliferation and differentiation are regulated by soluble factors

that feedback on self-renewal probabilities (Youssefpour et al. 2012; Lander et al. 2009; Kuncheet al. 2016). In particular, p_0 is positively regulated by a self-renewal promoter W with concentration C_w e.g., Wnt (Clevers et al. 2014; Schuijers and Clevers 2012).

The self-renewal fractions of CSC cells (φ_0) , Wnt-Hi (φ_1) and Wnt-Mod (φ_2) are modeled by:

$$P_0 = (1-p_2)\,(1-q_0)\cdot\frac{\chi_{00}C_{F0}}{1+\chi_{00}C_{F0}}\frac{\chi_0 C_F}{1+\chi_0 C_F}\frac{1}{1+\psi_0 C_B} \tag{4.15}$$

$$P_1 = (1-p_2)\,q_0\cdot\frac{\chi_1 C_F}{1+\chi_1 C_F}\frac{1}{1+\psi_1 C_B} \tag{4.16}$$

$$P_2 = \left(1-\tanh\tanh\ \frac{\left(C_W-\underline{C_W}\right)^2}{10}\right)\cdot\frac{\chi_2 C_F}{1+\chi_2 C_F}\frac{1}{1+\psi_2 C_B} \tag{4.17}$$

$$q_0 = q_1 = q_2 = \frac{1}{2}\left(1+\tanh\tanh\ \frac{C_W-\underline{C_W}}{1}\right), \tag{4.18}$$

where $\underline{C_W}$ is the characteristic Wnt level of Wnt-Mod. When $C_W = \underline{C_W}$, all Wnt-Mod self-renew. The tumor switches between oxidation ($q_0 = 0$) and glycolysis ($q_0 = 1$) based on the Wnt level.

The proliferation rates of CSC cells(φ_0) , Wnt-Hi (φ_1) and Wnt-Mod (φ_2) are modeled by:

$$\lambda_m = \underline{\lambda}\cdot\left[(1-q_0)\,\frac{(\beta_{Go}g+\beta_L L)\,n}{1+(\beta_{Go}g+\beta_L L)\,n}+q_0\frac{\beta_{GG}g}{1+\beta_{GG}g}\right] \tag{4.19}$$

$$\lambda_{m0} = \lambda_m\cdot\frac{\chi_{v00}C_{F0}}{1+\chi_{v00}C_{F0}}\frac{\chi_{v0}C_F}{1+\chi_{v0}C_F}\frac{1}{1+\psi_{v0}C_B} \tag{4.20}$$

$$\lambda_{m1} = \lambda_m\cdot\frac{\chi_{v1}C_F}{1+\chi_{v1}C_F}\frac{1}{1+\psi_{v1}C_B} \tag{4.21}$$

$$\lambda_{m2} = \lambda_m\cdot\frac{\chi_{v2}C_F}{1+\chi_{v2}C_F}\frac{1}{1+\psi_{v2}C_B}, \tag{4.22}$$

where $\underline{\lambda}$ is the base proliferation rate of all tumor cells. β_{Go} and β_L are the proliferation rate of glycolytic cells dependent on glucose (g) and lactate (L), respectively. β_{GG} is the proliferation of oxidative cells dependent on glucose. n is the oxygen concentration. χ_{v00} is the positive feedback gain of FGF20 (C_{F0}) on the proliferation rate of CSC. χ_{v0}, χ_{v1}, and

χ_{v2} are the positive feedback gain of FGF (C_F) on the proliferation rate of CSC, Wnt-Hi, and Wnt-Mod, respectively. ψ_{v0}, ψ_{v1}, and ψ_{v2} are the negative feedback gains from BMP (C_B).

Following [96], we use a generalized Gierer–Meinhardt model for Turing-type pattern formation. We assume that C_W is a short-range activator, and C_{WI} is a long-range inhibitor of C_W, e.g., Dkk. The system of reaction–diffusion equations are as follow:

$$\begin{aligned}
&\frac{\partial C_W}{\partial t} + \nabla \cdot (u_w C_W) = D_W \Delta C_W + \underline{\gamma} Src_W \\
&Src_W = P \cdot (p_W + \lambda_F C_F) \frac{C_W^2}{C_{WI}} + P \cdot p_W^B + p_W^S (1 - \varphi_T) - d_W C_W,
\end{aligned} \tag{4.23}$$

$$\begin{aligned}
&\frac{\partial C_{WI}}{\partial t} + \nabla \cdot (u_w C_{WI}) = D_{WI} \Delta C_{WI} + \underline{\gamma} Src_{WI} \\
&Src_{WI} = P \cdot p_{WI} C_W^2 + p_{WI}^S (1 - \varphi_T) - d_{WI} C_{WI},
\end{aligned} \tag{4.24}$$

$$P = (k_0 + k_1 n + k_2 g + k_3 L) (k_4 \varphi_0 + (1 - k_4) (\varphi_1 + \varphi_2)), \tag{4.25}$$

where $\underline{\gamma}$ is the reaction rate. D_W and D_{WI} are the diffusivity of Wnt and Dkk, respectively. D_W and D_{WI} are the natural decay of Wnt and Dkk, respectively.

P is the production rate of both Wnt and Dkk. k_0 is the base production rate. k_1, k_2, and k_3 are the production rate dependent on nutrient(n), glucose (g), and lactate (L), respectively. k_4 balances the production between CSC (φ_0) and non-CSC ($\varphi_1 + \varphi_2$). For Wnt, p_W is the base nonlinear production rate, which is increased by FGF ($\lambda_F C_F$). p_W^B is the background Wnt production in the tumor. p_W^S and p_{WI}^S are the stromal production rate of Wnt and Dkk, respectively.

We assume that negative feedback regulators FGF (C_F, C_{F0}) and BMP diffuse rapidly, and

the time derivatives and advection terms may be neglected. Note that C_F is required by all tumor cells and C_{F0} is required by CSC. The concentration of C_F, C_{F0} and BMP satisfy quasi-steady-state equations as follow:

FGF (C_F and C_{F0})

$$\begin{aligned} 0 &= D_F \Delta C_F + p_F \left(\varphi_T - \varphi_D\right) + p_F^S \left(1 - \varphi_T\right) - d_F C_F \\ 0 &= D_{F0} \Delta C_{F0} + p_{F0} \left(\varphi_0\right) + p_{F0}^{12} \left(\varphi_1 + \varphi_2\right) - d_{F0} C_{F0}, \end{aligned} \tag{4.26}$$

where D_F and D_{F0} are the diffusivities, d_F and d_{F0} are the natural decay rates. p_F is the production rate of C_F by all tumor cells, p_F^S is the production rate of C_F by the stroma. C_{F0} is produced by CSC at a rate of p_{F0}, and non-CSC at a rate of p_{F0}^{12}.

BMP (C_B):

$$0 = D_B \Delta C_B + p_B \left(\varphi_T - \varphi_D\right) - d_B C_B, \tag{4.27}$$

where D_B, p_B, and d_B are the diffusivity, production rate by all tumor cells, and natural decay rate, respectively.

In addition, we use similar idea to govern the oxygen concentration (n), the glucose concentration (g) and the lactate concentration (L), because their diffusion occurs on a significantly faster time scale cell (e.g., minutes) than the cell proliferation (e.g., days or more). Thus, the quasi-steady equations can be given as follow:

Oxygen concentration (n):

$$0 = D_n \Delta n - u_n \left(1 - q_0\right) \left(\varphi_T - \varphi_D\right) n + p_n Q \left(1 - \varphi_T\right) \left(\underline{n} - n\right), \tag{4.28}$$

where D_n and d_n are the diffusivity and natural decay rate, respectively. u_n is the uptakes

rate by oxidative tumor cells charactered by $(1-q_0)$. $Q(\varphi_T) \approx 1-\varphi_T$ approximates the characteristic function of the stroma. p_n is the nutrient supply rates from the microenvironment. $\underline{n}$ is the nutrient concentration in the microenvironment.

The glucose concentration (g):

$$0 = D_g \Delta g - u_g \left(\alpha_g q_0 + \alpha_o \left(1-q_0\right)\right)\left(\varphi_T - \varphi_D\right) g + \left(p_g^s Q\left(1-\varphi_T\right) + p_g^v \cdot C\right)\left(\underline{g} - g\right), \tag{4.29}$$

where D_g and d_g are the diffusivity and natural decay rate, respectively. u_g is the uptakes rate by oxidative tumor cells characterized by $\alpha_g q_0$ and glycolytic tumor cells characterized by $\alpha_o\left(1-q_0\right)$. $Q(\varphi_T) \approx 1-\varphi_T$ approximates the characteristic function of the stroma. p_g^s is the glucose production rates from the stroma. p_g^v is the glucose supply rates from the vessels. C is the continuous variable that describe vessel from angiogensis model. $\underline{g}$ is the nutrient concentration in the microenvironment.

The lactate concentration (L):

$$\begin{aligned} 0 = {} & D_L \Delta L - u_L\left(1-q_0\right)\left(\varphi_T - \varphi_D\right) L + p_L \cdot 2 u_G \alpha_g g \cdot q_0\left(\varphi_T - \varphi_D\right) \\ & + p_L^h H\left(\widetilde{n_L} - n\right)\left(\varphi_T - \varphi_D\right), \end{aligned} \tag{4.30}$$

where D_L and d_L are the diffusivity and natural decay rate, respectively. u_L is the uptakes rate by oxidative tumor cells characterized by $1-q_0$. p_L is the production rate by glycolytic tumor cells characterized by q_0. When one molecule of glucose is consumed, two molecules of lactate are produced $(2u_G\alpha_g g)$. p_L^h is the production rate by hypoxic tumor cells, where the oxygen level is less than a threshold $\widetilde{n_L}$. $H(x)$ is the Heaviside function.

Modified tumor angiogenic factor (f):

The model for tumor angiogenic factor(f) is different with what we described in Chapter.3.

Here, (f) is produced in the background, by glycolytic Wnt-Hi cells, and by hypoxic tumor cells (when nutrient is below a threshold, e.g. half the level in the stroma).

$$\frac{\partial f}{\partial t} = D_f \Delta f - (\gamma_f + u_f \cdot C) f + (p_f^0 + p_f^1 \varphi_1 + p_f^h (\varphi_T - \varphi_T) H(\widetilde{n_f} - n))(1 - f) \quad (4.31)$$

where D_f and γ_f are the diffusivity and natural decay rate, respectively. u_f is the uptakes rate by vessel. p_f^0 is the production rate by background. p_f^1 is the production rate by Wnt-Hi cells. . p_f^h is the production rate by hypoxic tumor cells, where the oxygen level is less than a threshold $\widetilde{n_f}$. $H(x)$ is the Heaviside function.

Finally, to close the model, we need to couple the angiogenesis model and the tumor growth model. In our tumor growth model, the tumor dynamics is strongly dependent on the glucose (g) (See Eqs. (4.29)). The glucose (g) , in turn , is released by vessel C that computed from angiogenesis model. The location of C depends on the TAF distribution. This makes the problem fully coupled.

Based on Chapter.3, the vessels are resolved to full scale and

Table 4.1: Parameters of the tumor growth model in dimensionless units.

Parameter	**Description**	**Value**
M	Cell mobility	10
ϵ	Diffuse interfacial thickness	0.05
γ	Adhesion force	-0.3
$\underline{\gamma}$	Reaction rate	25.0
$\underline{\lambda}$	Base division rate for viable cells	0.5
β_{GG}	Glycolytic cells utilizing glucose	1.0
β_{Go}	OXPHOS cells utilizing glucose	3.0
β_L	OXPHOS cells utilizing lactate	5.0

Continued on next page

Table 4.1 – continued from previous page

Parameter	Description	Value
χ_{00}	Positive gain from FGF20 on p_0	40
χ_{10}	Positive gain from FGF20 on Wnt-Hi switching to CSC	0.04
χ_{20}	Positive gain from FGF20 on Wnt-Mod switching to CSC	0.04
χ_0	Positive gain from FGF20 on p_0	40
χ_1	Positive gain from FGF20 on Wnt-Hi switching to CSC	0.04
χ_2	Positive gain from FGF20 on Wnt-Mod switching to CSC	0.04
ψ_0	Negative gain on p_0	0.1
ψ_1	Negative gain on p_1	1.0
ψ_2	Negative gain on p_2	0.1
χ_{v00}	Positive gain from FGF20 on λ_m for CSC	100
χ_{v0}	Positive gain from FGF20 on λ_m for 0-cells	10
χ_{v1}	Positive gain from FGF20 on λ_m for 1-cells	15
χ_{v2}	Positive gain from FGF20 on λ_m for 2-cells	12
ψ_{v0}	Negative gain on λ_m for 0-cells	0.0
ψ_{v1}	Negative gain on λ_m for 1-cells	1.0
ψ_{v2}	Negative gain on λ_m for 2-cells	0.1
D_{F0}	Diffusivity of FGF20	1.0
D_F	Diffusivity of FGF	1.0
D_B	Diffusivity of BMP	1.0
p_{F0}	Production of FGF20 by stem cells	6.0
p_{F0}^{12}	Production of FGF by non-stem cells	0.5
p_F	Production of FGF20 by tumor cells	1.0
p_B	Production of BMP by tumor cells	1.0
p_F^S	Production of FGF by stroma	2.0

Continued on next page

Table 4.1 – continued from previous page

Parameter	Description	Value
d_{F0}	Natural decay of FGF20	1.0
D_n	Diffusivity of oxygen	1.0
D_g	Diffusivity of glucose	2.0
D_L	Diffusivity of lactate	1.0
$\widetilde{n_0}$	0-cell oxygen threshold of necrosis	0.35
$\widetilde{n_1}$	1-cell oxygen threshold of necrosis	0.05
$\widetilde{n_2}$	2-cell oxygen threshold of necrosis	0.05
λ_{n0}	Necrosis rate of 0-cells	0.2
λ_{n1}	Necrosis rate of 1-cells	0.2
λ_{n2}	Necrosis rate of 2-cells	0.2
u_n	Oxygen uptake rate by OXPHOS cells	1.0
u_g	Glucose uptake rate by cells	1.0
u_L	Oxygen uptake rate by OXPHOS cells	1.0
p_n	Oxygen production by host	1.0
$\underline{n}$	Oxygen level in stroma	1.0
$\underline{g}$	Glucose level in stroma	1.0
$\widetilde{n_L}$	Hypoxic threshold for lactate production	0.05
p_L^h	Production of lactate by hypoxic cells	1.0
p_L^g	Production of lactate by glycolytic cells	1.0
p_g	Production of glucose by stroma	1.0
p_n	Oxygen production by host	1.0
α_o	Fraction of uptake by OXPHOS cells	0.0
α_g	Fraction of uptake by glycolytic cells	1.0
D_W	Diffusivity of Wnt	0.25

Continued on next page

Table 4.1 – continued from previous page

Parameter	Description	Value
D_{WI}	Diffusivity of Wnt inhibitor	6.25
p_W	Production rate of Wnt	2.5
λ_F	Upregulated production of Wnt by FGF	2.0
k_4	Fraction of Wnt Production by SCs	0.3
$\underline{C_W}$	Average Wnt signaling level	6.0
p_W^B	Production rate of Wnt by viable tumor cells	1.0
p_W^S	Production rate of Wnt by stroma	1.0
p_{WI}	Production rate of Wnt Inhibitor	1.0
p_{WI}^S	Production rate of Wnt Inhibitor by stroma	0.0
d_w	Natural decay of Wnt	1.0
d_{WI}	Natural decay of Wnt Inhibitor	1.0
k_0	Independent production of Wnt	0.1
k_1	Oxygen dependent production of Wnt	0.4
k_2	Glucose dependent production of Wnt	0.4
k_3	Lactate dependent production of Wnt	1.0
D_f	Diffusivity of Angiogenic factor	1.0
γ_f	Natural decay of Angiogenic factor	0.35
u_f	Angiogenic factor uptake rate by cells	15
p_f^h	Production of Angiogenic factor by hypoxic cells	10
p_f^0	Production of Angiogenic factor by host	10
p_f^1	Production of Angiogenic factor by Wnt-Hi cells	10
$\widetilde{n_f}$	Hypoxic threshold for Angiogenic factor production	0.1

4.4 Numerical Results

To initialize our hybrid model with a realistic vascular network, we extract the initial vasculature from fluorescent images of the VMT device by segmenting the fluorescent images of the VMT device using a combination of image processing techniques, such as thresholding, morphological operations, and skeletonization [70]. The segmented vasculature is then discretized and mapped onto the computational domain, providing a realistic starting point for our simulations. The initial condition of our vasculature network obtained from the fluorescent image of a VMT chamber is shown in Fig. 4.3.

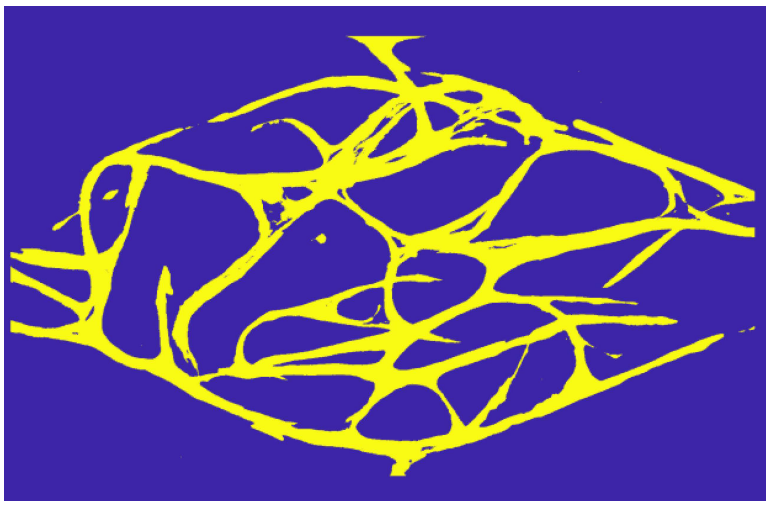

Figure 4.3: Pre-existing vessel network image extracted from VMT device.

To investigate the model's performance on the pre-existing complex vascular domain, we first conduct a simulation of our angiogenesis model on the previously extracted VMT domain. The model used here are described in Chapter.3.

The grid parameters are as follows: the domain is $\Omega = (0, 1491) \times (0, 1491)$ with uniform grid 1491×1491 which is the pixel of the image. The boundary conditions the simulation is zero-flux conditions. As a simulation time period, the interval $(0, T)$ with $T = 40$ is considered

and the size of time step is given by $\Delta t = 2.0 \times 10^{-4}$. The parameter values in dimensionless units used in the computations are summarized in Table.4.2. The computational simulation involves a finite difference scheme in a MATLAB script.

Table 4.2: Parameters of the angiogenesis model in dimensionless units.

parameter	Description	Value
D	tumor angiogenic factor diffusion coefficient	400.0
f_{hyc}	maximum tumor angiogenic factor concentration in the tissue	1.0
P	tumor angiogenic factor production by HYCs	350
R	average cell radius	5.0
U_u	tumor angiogenic factor endothelial cell uptake	21.875
U_d	tumor angiogenic factor natural decay	0.35
λ	interface width	1.0
M	mobility	0.0975
χ	chemotatic constant of tip endothelial cells	250.47
c_{act}	condition for TEC activation	0.9
f_{act}	condition for TEC activation	0.01
δ_4	Dll-4 radius of action	28
δ_{nox}	condition for HYC deactivation	10

In Fig. 4.4, the time evolution of tumor angiogenesis simulations obtained from a complex domain are depicted. The simulation begins with three clusters of hypoxic tumor cells releasing TAFs, which triggers angiogenesis, as shown at $t = 0$. At time $t = 1$, we observe that the activation of TECs occurs when the TAFs diffuses throughout the hypoxic region and infiltrate the initial capillary. Note that all TECs are spaced apart from each other as dictated by the lateral inhibition mechanism. The activated TECs migrate following the chemotactic direction and the filopodia (red dot) are developed to detect nearby capillaries. At time $t = 2$, as vessels grow , TECs create new branches and bifurcations, leading to the formation of a tree-like network . Endothelial cells consume angiogenic factor and tumor

cells that are close to capillaries become normoxic and stop releasing TAF. Thus, a small number of TECs are deactivated due to the low level of TAFs. Furthermore, when the filopodia detect the presence of a capillary, TECs alter their movement direction towards the detected capillary. This event triggers the formation of anastomoses, eventually leading to the deactivation of the TECs. At time $t = 3$, as the vasculature network continues to develop, the frequency of anastomosis events increases rapidly. Consequently, the tree-like network gradually evolves to a mesh-like one with loops that facilitate blood flow.

The simulations demonstrate the ability of our angiogenesis model to capture the key features of angiogenesis, such as the activation and migration of TECs, the formation of new capillary branches, and the influence of angiogenic factor gradients on the vascular morphology.

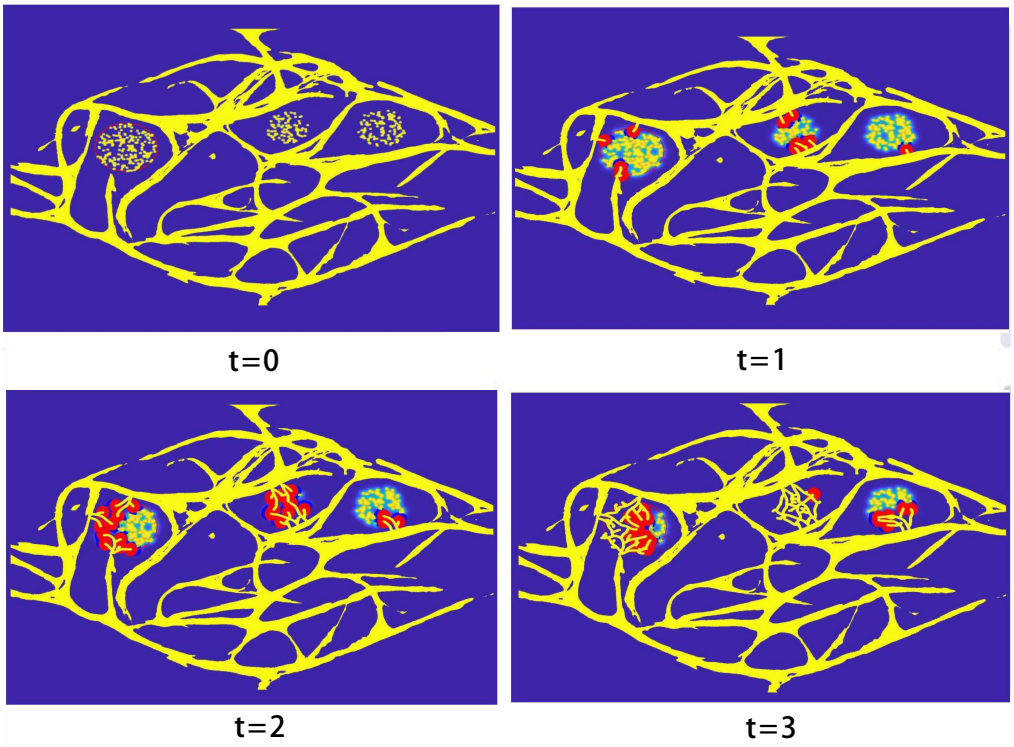

Figure 4.4: The evolution of the formation of angiogenesis in VMT

Next, we simulate the full tumor-induced angiogenesis model described in the previous Section 4.3. The governing equations of tumor growth model are complex high-order nonlinear

partial differential equations, and require sophisticated numerical methods to avoid severe time-step restrictions for numerical stability, to accurately resolve phenomena on various spatial scales, and to solve the equations efficiently. Thus, the equations of tumor growth model and continue part of angiogenesis model are solved using the mass-conservative adaptive, FAS (Full Approximation Storage), nonlinear multigrid method that we built and presented in Chapter.2. The time-dependent equations are discretized by an semi-implicit second-order Crank–Nicholson scheme. Spatial derivatives are discretized using central difference approximations. We apply homogeneous Neumann boundary conditions for tumor cell speciesl, C_w, and C_{WI} in all boundaries. The concentration of n , C_F, C_{F0}, BMP, g, and L satisfy the Dirichlet condition at all boundaries. The grid parameters are as follows: the domain is $\Omega = (-20, 20) \times (-20, 20)$ with root level grid of size 32^2. Three level of refinement are used so that the finest level has the effective resolution of a uniform grid 256×256. We set the time step $\Delta t = 1.0 \times 10^{-3}$. Moreover, the initial condition is shown in Fig. 4.5. The parameter values in dimensionless units used in the computations are summarized in Table.4.1.

Fig. 4.6 presents a time-series of the tumor-induced angiogenesis simulations performed on the complex vascular domain extracted from the VMT platform. At $t = 4$, the tumor cells (represented by the green isosurface) have released sufficient TAFs to activate several TECs within the nearby vessels. These activated TECs begin to sprout and migrate through the vessel network, guided by the gradients of TAFs. The chemotactic response of the TECs to the TAF gradients is a key driver of the angiogenic process, directing the growth of new capillary branches towards the tumor.

As the simulation progresses ($t = 8$, $t = 10$, and $t = 12$), the activated TECs continue to lead the sprouting and elongation of new capillary branches, forming a dense network of vessels that penetrate the tumor mass. The branching and anastomosis of the growing vessels result in the emergence of a highly connected, network-like vascular pattern. This

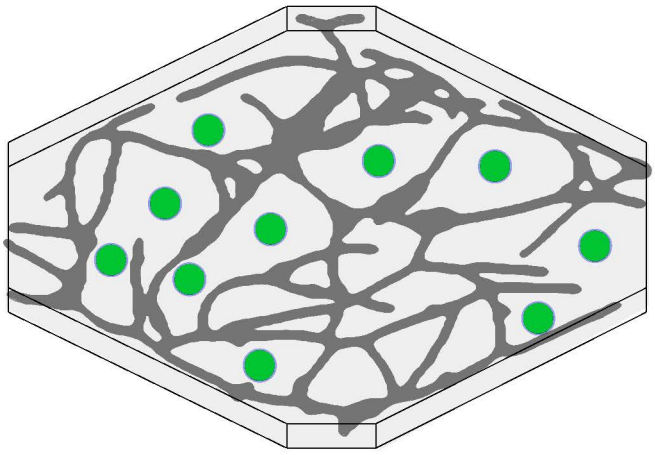

Figure 4.5: The initial condition of the tumor-induced angiogenesis model in the VMT platform. Vessel in grey, the tumor $\varphi = 0.5$ isosurface in green. 10 cluster of tumors are seeded in the device.

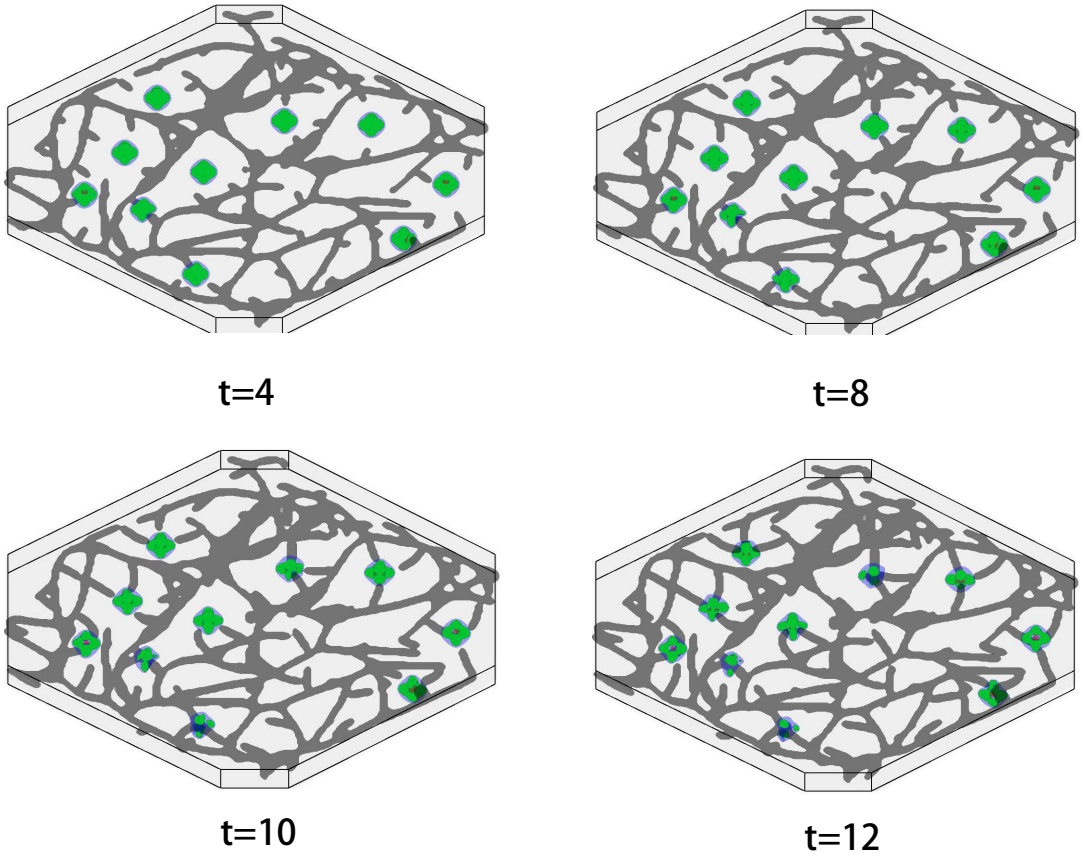

Figure 4.6: The evolution of the tumor-induced angiogenesis in the VMT platform

evolving vascular network is characterized by numerous loops and interconnections, which are essential for establishing adequate blood flow and nutrient delivery to the tumor.

Notably, the complex geometry of the initial vascular network, derived from the VMT platform, significantly influences the angiogenesis process. The new vessels must navigate through the intricate, tortuous paths of the pre-existing vasculature, adding to the complexity and realism of the simulation. The hybrid model successfully captures this interplay between the discrete TECs, continuous vessel dynamics, and the realistic vascular geometry, providing valuable insights into the spatiotemporal evolution of tumor-induced angiogenesis.

4.5 Summary and future work

We presented a hybrid model for coupled tumor growth and angiogenesis. The model resolves the capillaries to full scale and simulate long-term dynamics of angiogenesis. Our results demonstrate the capability of our hybrid mathematical model to simulate the intricate dynamics of tumor-induced angiogenesis from a complex pre-existing vasculature network (VMT). The simulations demonstrate how the discrete tip endothelial cells (TECs) activated and guided by chemotactic cues from the TAF gradients, lead the sprouting and migration of new capillary branches towards the hypoxic tumor regions.

Notably, the incorporation of discrete filopodia agents allows TECs to sense and navigate towards nearby capillaries, facilitating the formation of anastomoses and the evolution of a connected, loop-rich vascular network. The model accurately represents the lateral inhibition process mediated by the Notch-Delta signaling pathway, which ensures an optimal patterning of the vascular network by suppressing the formation of excessive tip cells. The continuum phase-field approach for modeling capillary dynamics, coupled with the discrete TEC agents, effectively couple the interplay between continuous and discrete processes during angiogenesis.

However, it is important to acknowledge potential limitations of the current model. While the phase-field approach allows for the resolution of capillary-scale features, it may not fully capture the intricate dynamics of individual endothelial cells within the capillaries. Additionally, the model assumes a simplified representation of the tumor microenvironment, neglecting potential effects of other stromal components, such as pericytes, smooth muscle cells, and the extracellular matrix.

Future extensions of the model could incorporate additional biological mechanisms, such as the influence of haptotaxis, fluid flow, the role of stromal cells in vessel maturation, and the impact of mechanical forces on capillary remodeling. Furthermore, coupling the angio-

genesis model with a more comprehensive tumor growth model could provide insights into the interplay between vascular development and tumor progression, potentially informing therapeutic strategies that target both processes.

Overall, this hybrid mathematical model represents a valuable tool for studying the intricate dynamics of tumor angiogenesis, bridging the gap between cellular and tissue scales. By integrating biological mechanisms with computational modeling, it contributes to a deeper understanding of the complex processes involved in cancer progression and may aid in the development of more effective anti-angiogenic therapies.

Chapter 5

Conclusions

In this thesis, we have presented a comprehensive study on the mathematical modeling of tumor-induced angiogenesis, spanning from the fundamental concepts to the development of a novel hybrid model that integrates tumor growth and angiogenesis in a complex, realistic vascular network.

Chapter 1 introduced the significance of angiogenesis in cancer progression and the need for mathematical models to better understand these complex processes. We reviewed existing modeling approaches, including discrete, continuous, and hybrid models, and highlighted the gaps in current literature that our work aims to address.

In Chapter 2, we focused on a thermodynamically consistent mixture model for avascular solid tumor growth, which takes into account cell proliferation, death, cell-to-cell adhesion, and taxis-inducing chemical and molecular species. We developed a mass-conservative, adaptive, finite difference, nonlinear multigrid method to simulate the model efficiently and accurately. The numerical results demonstrated the model's ability to capture various tumor morphologies and the importance of mass conservation in maintaining numerical accuracy.

Chapter 3 introduced a multiscale model for angiogenesis growth based on the phase-field theory. The model incorporates the dynamics of capillaries, angiogenic factors, and tip endothelial cells (TECs), along with a discrete conceptualization of filopodia that enables TECs to sense their microenvironment. We presented numerical simulations that showcased the model's capability to simulate the formation of a connected, loop-rich vascular network from a simple initial vasculature.

Building upon the foundations laid in Chapters 2 and 3, Chapter 4 presented a hybrid mathematical model that integrates tumor growth and angiogenesis in a complex, realistic vascular network extracted from the vascularized microtumor (VMT) platform. The model combines continuum and discrete modeling approaches to capture the key biological processes involved in tumor angiogenesis. Our simulation results demonstrated the model's ability to recapitulate the complex dynamics of tumor-induced angiogenesis, including the activation and migration of TECs, the formation of new capillary branches, and the emergence of a connected vascular network.

While our hybrid mathematical model represents a significant advancement in the field, it is important to acknowledge its limitations. Future extensions of the model could incorporate additional biological mechanisms, such as the influence of haptotaxis, fluid flow, and mechanical forces on capillary remodeling. Coupling the angiogenesis model with a more comprehensive tumor growth model could provide further insights into the interplay between vascular development and tumor progression.

In conclusion, our work contributes to a deeper understanding of the complex processes involved in tumor angiogenesis by developing a series of mathematical models that span from avascular tumor growth to a hybrid model of tumor growth and angiogenesis in a realistic vascular network. By integrating biological knowledge with computational modeling, we can continue to unravel the intricacies of tumor angiogenesis and ultimately inform the development of more effective anti-angiogenic therapies. The models presented in this paper

provide a solid foundation for future research in this field and have the potential to make a significant impact on our understanding of cancer progression and treatment."

Bibliography

[1] P. M. Altrock, L. L. Liu, and F. Michor. The mathematics of cancer: integrating quantitative models. *Nature Reviews Cancer*, 15(12):730–745, 2015.

[2] D. Ambrosi and L. Preziosi. On the closure of mass balance models for tumor growth. *Mathematical Models and Methods in Applied Sciences*, 12(05):737–754, 2002.

[3] A. R. Anderson and M. A. Chaplain. Continuous and discrete mathematical models of tumor-induced angiogenesis. *Bulletin of mathematical biology*, 60(5):857–899, 1998.

[4] R. P. Araujo and D. S. McElwain. A history of the study of solid tumour growth: the contribution of mathematical modelling. *Bulletin of mathematical biology*, 66(5):1039–1091, 2004.

[5] D. Barbolosi, J. Ciccolini, B. Lacarelle, F. Barlési, and N. André. Computational oncology—mathematical modelling of drug regimens for precision medicine. *Nature reviews Clinical oncology*, 13(4):242–254, 2016.

[6] D. Basanta and A. R. Anderson. Homeostasis back and forth: an ecoevolutionary perspective of cancer. *Cold Spring Harbor perspectives in medicine*, 7(9), 2017.

[7] A. Beenken and M. Mohammadi. The fgf family: biology, pathophysiology and therapy. *Nature reviews Drug discovery*, 8(3):235–253, 2009.

[8] S. Bekisz and L. Geris. Cancer modeling: From mechanistic to data-driven approaches, and from fundamental insights to clinical applications. *Journal of Computational Science*, 46:101198, 2020.

[9] N. Bellomo, N. Li, and P. K. Maini. On the foundations of cancer modelling: selected topics, speculations, and perspectives. *Mathematical Models and Methods in Applied Sciences*, 18(04):593–646, 2008.

[10] K. Bentley, G. Mariggi, H. Gerhardt, and P. A. Bates. Tipping the balance: robustness of tip cell selection, migration and fusion in angiogenesis. *PLoS computational biology*, 5(10):e1000549, 2009.

[11] G. Bergers and L. E. Benjamin. Tumorigenesis and the angiogenic switch. *Nature reviews cancer*, 3(6):401–410, 2003.

[12] M. Bienz and H. Clevers. Linking colorectal cancer to wnt signaling. *Cell*, 103(2):311–320, 2000.

[13] R. Blanco and H. Gerhardt. Vegf and notch in tip and stalk cell selection. *Cold Spring Harbor perspectives in medicine*, 3(1), 2013.

[14] D. Bouïs, Y. Kusumanto, C. Meijer, N. H. Mulder, and G. A. Hospers. A review on pro- and anti-angiogenic factors as targets of clinical intervention. *Pharmacological Research*, 53(2):89–103, 2006.

[15] R. M. Bowen. Incompressible porous media models by use of the theory of mixtures. *International Journal of Engineering Science*, 18(9):1129–1148, 1980.

[16] T. Brabletz, A. Jung, K. Hermann, K. Günther, W. Hohenberger, and T. Kirchner. Nuclear overexpression of the oncoprotein β-catenin in colorectal cancer is localized predominantly at the invasion front. *Pathology-Research and Practice*, 194(10):701–704, 1998.

[17] T. Brabletz, A. Jung, S. Reu, M. Porzner, F. Hlubek, L. A. Kunz-Schughart, R. Knuechel, and T. Kirchner. Variable β-catenin expression in colorectal cancers indicates tumor progression driven by the tumor environment. *Proceedings of the National Academy of Sciences*, 98(18):10356–10361, 2001.

[18] H. Byrne, T. Alarcon, M. Owen, S. Webb, and P. Maini. Modelling aspects of cancer dynamics: a review. *Philosophical Transactions of the Royal Society A: Mathematical, Physical and Engineering Sciences*, 364(1843):1563–1578, 2006.

[19] H. Byrne and L. Preziosi. Modelling solid tumour growth using the theory of mixtures. *Mathematical medicine and biology: a journal of the IMA*, 20(4):341–366, 2003.

[20] J. W. Cahn and J. E. Hilliard. Free energy of a nonuniform system. i. interfacial free energy. *The Journal of chemical physics*, 28(2):258–267, 1958.

[21] P. Carmeliet and R. K. Jain. Angiogenesis in cancer and other diseases. *nature*, 407(6801):249–257, 2000.

[22] M. Chaplain. Avascular growth, angiogenesis and vascular growth in solid tumours: The mathematical modelling of the stages of tumour development. *Mathematical and computer modelling*, 23(6):47–87, 1996.

[23] L.-Q. Chen. Phase-field models for microstructure evolution. *Annual review of materials research*, 32(1):113–140, 2002.

[24] H. Clevers. Wnt/β-catenin signaling in development and disease. *Cell*, 127(3):469–480, 2006.

[25] H. Clevers, K. M. Loh, and R. Nusse. An integral program for tissue renewal and regeneration: Wnt signaling and stem cell control. *science*, 346(6205):1248012, 2014.

[26] J. R. Crawshaw, J. A. Flegg, M. O. Bernabeu, and J. M. Osborne. Mathematical models of developmental vascular remodelling: A review. *PLoS Computational Biology*, 19(8):e1011130, 2023.

[27] V. Cristini, H. B. Frieboes, X. Li, J. S. Lowengrub, P. Macklin, S. Sanga, S. M. Wise, and X. Zheng. Nonlinear modeling and simulation of tumor growth. *Selected topics in cancer modeling: genesis, evolution, immune competition, and therapy*, pages 1–69, 2008.

[28] V. Cristini, X. Li, J. S. Lowengrub, and S. M. Wise. Nonlinear simulations of solid tumor growth using a mixture model: invasion and branching. *Journal of mathematical biology*, 58(4):723–763, 2009.

[29] V. Cristini, J. Lowengrub, and Q. Nie. Nonlinear simulation of tumor growth. *Journal of mathematical biology*, 46:191–224, 2003.

[30] M. G. Dallinga, S. E. Boas, I. Klaassen, R. H. Merks, C. J. van Noorden, and R. O. Schlingemann. Tip cells in angiogenesis. *eLS*, pages 1–10, 2015.

[31] F. De Smet, I. Segura, K. De Bock, P. J. Hohensinner, and P. Carmeliet. Mechanisms of vessel branching: filopodia on endothelial tip cells lead the way. *Arteriosclerosis, thrombosis, and vascular biology*, 29(5):639–649, 2009.

[32] R. del Toro, C. Prahst, T. Mathivet, G. Siegfried, J. S. Kaminker, B. Larrivee, C. Breant, A. Duarte, N. Takakura, A. Fukamizu, et al. Identification and functional analysis of endothelial tip cell–enriched genes. *Blood, The Journal of the American Society of Hematology*, 116(19):4025–4033, 2010.

[33] P. Dogra, J. D. Butner, Y.-l. Chuang, S. Caserta, S. Goel, C. J. Brinker, V. Cristini, and Z. Wang. Mathematical modeling in cancer nanomedicine: a review. *Biomedical microdevices*, 21:1–23, 2019.

[34] M. Dorraki, A. Fouladzadeh, A. Allison, C. S. Bonder, and D. Abbott. Angiogenic networks in tumors—insights via mathematical modeling. *IEEE Access*, 8:43215–43228, 2020.

[35] H. Emmerich. *The diffuse interface approach in materials science: thermodynamic concepts and applications of phase-field models*, volume 73. Springer Science & Business Media, 2003.

[36] H. Enderling and M. AJ Chaplain. Mathematical modeling of tumor growth and treatment. *Current pharmaceutical design*, 20(30):4934–4940, 2014.

[37] J. Faix and K. Rottner. The making of filopodia. *Current opinion in cell biology*, 18(1):18–25, 2006.

[38] W. Feng, Z. Guo, J. S. Lowengrub, and S. M. Wise. A mass-conservative adaptive fas multigrid solver for cell-centered finite difference methods on block-structured, locally-cartesian grids. *Journal of Computational Physics*, 352:463–497, 2018.

[39] J. Folkman et al. Tumor angiogenesis: therapeutic implications. *N Engl j Med*, 285(21):1182–1186, 1971.

[40] H. B. Frieboes, F. Jin, Y.-L. Chuang, S. M. Wise, J. S. Lowengrub, and V. Cristini. Three-dimensional multispecies nonlinear tumor growth—ii: tumor invasion and angiogenesis. *Journal of theoretical biology*, 264(4):1254–1278, 2010.

[41] A. Friedman. Mathematical analysis and challenges arising from models of tumor growth. *Mathematical Models and Methods in Applied Sciences*, 17(supp01):1751–1772, 2007.

[42] H. Gerhardt, M. Golding, M. Fruttiger, C. Ruhrberg, A. Lundkvist, A. Abramsson, M. Jeltsch, C. Mitchell, K. Alitalo, D. Shima, et al. Vegf guides angiogenic sprouting utilizing endothelial tip cell filopodia. *The Journal of cell biology*, 161(6):1163–1177, 2003.

[43] I. G. Gonçalves and J. M. García-Aznar. Hybrid computational models of multicellular tumour growth considering glucose metabolism. *Computational and Structural Biotechnology Journal*, 2023.

[44] P. B. Gupta, C. M. Fillmore, G. Jiang, S. D. Shapira, K. Tao, C. Kuperwasser, and E. S. Lander. Stochastic state transitions give rise to phenotypic equilibrium in populations of cancer cells. *Cell*, 146(4):633–644, 2011.

[45] S. J. Hachey and C. C. Hughes. Applications of tumor chip technology. *Lab on a Chip*, 18(19):2893–2912, 2018.

[46] S. J. Hachey, S. Movsesyan, Q. H. Nguyen, G. Burton-Sojo, A. Tankazyan, J. Wu, T. Hoang, D. Zhao, S. Wang, M. M. Hatch, et al. An in vitro vascularized micro-tumor model of human colorectal cancer recapitulates in vivo responses to standard-of-care therapy. *Lab on a Chip*, 21(7):1333–1351, 2021.

[47] D. Hanahan. Hallmarks of cancer: new dimensions. *Cancer discovery*, 12(1):31–46, 2022.

[48] D. Hanahan and R. A. Weinberg. The hallmarks of cancer. *cell*, 100(1):57–70, 2000.

[49] D. Hanahan and R. A. Weinberg. Hallmarks of cancer: the next generation. *cell*, 144(5):646–674, 2011.

[50] M. Hellström, L.-K. Phng, J. J. Hofmann, E. Wallgard, L. Coultas, P. Lindblom, J. Alva, A.-K. Nilsson, L. Karlsson, N. Gaiano, et al. Dll4 signalling through notch1 regulates formation of tip cells during angiogenesis. *Nature*, 445(7129):776–780, 2007.

[51] S. P. Herbert, J. Y. Cheung, and D. Y. Stainier. Determination of endothelial stalk versus tip cell potential during angiogenesis by h2. 0-like homeobox-1. *Current Biology*, 22(19):1789–1794, 2012.

[52] S. P. Herbert and D. Y. Stainier. Molecular control of endothelial cell behaviour during blood vessel morphogenesis. *Nature reviews Molecular cell biology*, 12(9):551–564, 2011.

[53] D. J. Hicklin and L. M. Ellis. Role of the vascular endothelial growth factor pathway in tumor growth and angiogenesis. *Journal of clinical oncology*, 23(5):1011–1027, 2005.

[54] D. A. Hormuth, C. M. Phillips, C. Wu, E. A. Lima, G. Lorenzo, P. K. Jha, A. M. Jarrett, J. T. Oden, and T. E. Yankeelov. Biologically-based mathematical modeling of tumor vasculature and angiogenesis via time-resolved imaging data. *Cancers*, 13(12):3008, 2021.

[55] J. Humphrey. Constrained mixture models of soft tissue growth and remodeling–twenty years after. *Journal of Elasticity*, 145(1-2):49–75, 2021.

[56] X. Jiang, J. Wang, X. Deng, F. Xiong, S. Zhang, Z. Gong, X. Li, K. Cao, H. Deng, Y. He, et al. The role of microenvironment in tumor angiogenesis. *Journal of Experimental & Clinical Cancer Research*, 39(1):1–19, 2020.

[57] R. Kobayashi. A brief introduction to phase field method. In *AIP Conference Proceedings*, volume 1270, pages 282–291. American Institute of Physics, 2010.

[58] P. Koumoutsakos, I. Pivkin, and F. Milde. The fluid mechanics of cancer and its therapy. *Annual review of fluid mechanics*, 45:325–355, 2013.

[59] C. Y. Lee and V. L. Bautch. Ups and downs of guided vessel sprouting: the role of polarity. *Physiology*, 26(5):326–333, 2011.

[60] X. Li, V. Cristini, Q. Nie, and J. S. Lowengrub. Nonlinear three-dimensional simulation of solid tumor growth. *DISCRETE AND CONTINUOUS DYNAMICAL SYSTEMS SERIES B*, 7(3):581, 2007.

[61] E. A. Logsdon, S. D. Finley, A. S. Popel, and F. M. Gabhann. A systems biology view of blood vessel growth and remodelling. *Journal of cellular and molecular medicine*, 18(8):1491–1508, 2014.

[62] J. S. Lowengrub, H. B. Frieboes, F. Jin, Y.-L. Chuang, X. Li, P. Macklin, S. M. Wise, and V. Cristini. Nonlinear modelling of cancer: bridging the gap between cells and tumours. *Nonlinearity*, 23(1):R1, 2009.

[63] D. F. Martin and K. L. Cartwright. *Solving Poisson's equation using adaptive mesh refinement*. Citeseer, 1996.

[64] P. K. Mattila and P. Lappalainen. Filopodia: molecular architecture and cellular functions. *Nature reviews Molecular cell biology*, 9(6):446–454, 2008.

[65] J. Metzcar, Y. Wang, R. Heiland, and P. Macklin. A review of cell-based computational modeling in cancer biology. *JCO clinical cancer informatics*, 2:1–13, 2019.

[66] F. Michor, Y. Iwasa, and M. A. Nowak. Dynamics of cancer progression. *Nature reviews cancer*, 4(3):197–205, 2004.

[67] J. D. Nagy. The ecology and evolutionary biology of cancer: a review of mathematical models of necrosis and tumor cell diversity. *Math. Biosci. Eng*, 2(2):381–418, 2005.

[68] J. T. Oden, A. Hawkins, and S. Prudhomme. General diffuse-interface theories and an approach to predictive tumor growth modeling. *Mathematical Models and Methods in Applied Sciences*, 20(03):477–517, 2010.

[69] N. G. Pantelelis and A. E. Kanarachos. The parallel block adaptive multigrid method for the implicit solution of the euler equations. *International journal for numerical methods in fluids*, 22(5):411–428, 1996.

[70] D. T. Phan, X. Wang, B. M. Craver, A. Sobrino, D. Zhao, J. C. Chen, L. Y. Lee, S. C. George, A. P. Lee, and C. C. Hughes. A vascularized and perfused organ-on-a-chip platform for large-scale drug screening applications. *Lab on a Chip*, 17(3):511–520, 2017.

[71] L. Preziosi and A. Tosin. Multiphase modelling of tumour growth and extracellular matrix interaction: mathematical tools and applications. *Journal of mathematical biology*, 58:625–656, 2009.

[72] C. W. Pugh and P. J. Ratcliffe. Regulation of angiogenesis by hypoxia: role of the hif system. *Nature medicine*, 9(6):677–684, 2003.

[73] V. Quaranta, A. M. Weaver, P. T. Cummings, and A. R. Anderson. Mathematical modeling of cancer: the future of prognosis and treatment. *Clinica Chimica Acta*, 357(2):173–179, 2005.

[74] M. Rajabi and S. A. Mousa. The role of angiogenesis in cancer treatment. *Biomedicines*, 5(2):34, 2017.

[75] R. C. Rockne, A. Hawkins-Daarud, K. R. Swanson, J. P. Sluka, J. A. Glazier, P. Macklin, D. A. Hormuth, A. M. Jarrett, E. A. Lima, J. T. Oden, et al. The 2019 mathematical oncology roadmap. *Physical biology*, 16(4):041005, 2019.

[76] T. Roose, S. J. Chapman, and P. K. Maini. Mathematical models of avascular tumor growth. *SIAM review*, 49(2):179–208, 2007.

[77] G. Schaller and M. Meyer-Hermann. Continuum versus discrete model: a comparison for multicellular tumour spheroids. *Philosophical Transactions of the Royal Society A: Mathematical, Physical and Engineering Sciences*, 364(1843):1443–1464, 2006.

[78] A. Sobrino, D. T. Phan, R. Datta, X. Wang, S. J. Hachey, M. Romero-López, E. Gratton, A. P. Lee, S. C. George, and C. C. Hughes. 3d microtumors in vitro supported by perfused vascular networks. *Scientific reports*, 6(1):31589, 2016.

[79] H. Sung, J. Ferlay, R. L. Siegel, M. Laversanne, I. Soerjomataram, A. Jemal, and F. Bray. Global cancer statistics 2020: Globocan estimates of incidence and mortality worldwide for 36 cancers in 185 countries. *CA: a cancer journal for clinicians*, 71(3):209–249, 2021.

[80] N. Tang, L. Wang, J. Esko, F. J. Giordano, Y. Huang, H.-P. Gerber, N. Ferrara, and R. S. Johnson. Loss of hif-1α in endothelial cells disrupts a hypoxia-driven vegf autocrine loop necessary for tumorigenesis. *Cancer cell*, 6(5):485–495, 2004.

[81] G. Thurston and J. Kitajewski. Vegf and delta-notch: interacting signalling pathways in tumour angiogenesis. *British Journal of Cancer*, 99(8):1204–1209, 2008.

[82] R. D. Travasso, E. Corvera Poiré, M. Castro, J. C. Rodrguez-Manzaneque, and A. Hernández-Machado. Tumor angiogenesis and vascular patterning: a mathematical model. *PloS one*, 6(5):e19989, 2011.

[83] P. Van Liedekerke, M. Palm, N. Jagiella, and D. Drasdo. Simulating tissue mechanics with agent-based models: concepts, perspectives and some novel results. *Computational particle mechanics*, 2:401–444, 2015.

[84] P. Vaupel and A. Mayer. Hypoxia in cancer: significance and impact on clinical outcome. *Cancer and Metastasis Reviews*, 26:225–239, 2007.

[85] V. Vavourakis, P. A. Wijeratne, R. Shipley, M. Loizidou, T. Stylianopoulos, and D. J. Hawkes. A validated multiscale in-silico model for mechano-sensitive tumour angiogenesis and growth. *PLoS computational biology*, 13(1):e1005259, 2017.

[86] G. Vilanova, I. Colominas, and H. Gomez. Capillary networks in tumor angiogenesis: From discrete endothelial cells to phase-field averaged descriptions via isogeometric analysis. *International journal for numerical methods in biomedical engineering*, 29(10):1015–1037, 2013.

[87] G. Vilanova, I. Colominas, and H. Gomez. A mathematical model of tumour angiogenesis: growth, regression and regrowth. *Journal of The Royal Society Interface*, 14(126):20160918, 2017.

[88] J. A. Weis, M. I. Miga, L. R. Arlinghaus, X. Li, A. B. Chakravarthy, V. Abramson, J. Farley, and T. E. Yankeelov. A mechanically coupled reaction–diffusion model for predicting the response of breast tumors to neoadjuvant chemotherapy. *Physics in Medicine & Biology*, 58(17):5851, 2013.

[89] D. A. Winters, T. Soukup, N. Sevdalis, J. S. Green, and B. W. Lamb. The cancer multidisciplinary team meeting: in need of change? history, challenges and future perspectives. *BJU international*, 128(3):271–279, 2021.

[90] S. Wise, J. Kim, and J. Lowengrub. Solving the regularized, strongly anisotropic cahn–hilliard equation by an adaptive nonlinear multigrid method. *Journal of Computational Physics*, 226(1):414–446, 2007.

[91] S. M. Wise, J. S. Lowengrub, H. B. Frieboes, and V. Cristini. Three-dimensional multispecies nonlinear tumor growth—i: model and numerical method. *Journal of theoretical biology*, 253(3):524–543, 2008.

[92] J. Xu, G. Vilanova, and H. Gomez. A mathematical model coupling tumor growth and angiogenesis. *PloS one*, 11(2):e0149422, 2016.

[93] H. Yan, A. Konstorum, and J. S. Lowengrub. Three-dimensional spatiotemporal modeling of colon cancer organoids reveals that multimodal control of stem cell self-renewal is a critical determinant of size and shape in early stages of tumor growth. *Bulletin of mathematical biology*, 80(5):1404–1433, 2018.

[94] A. Yin, D. J. A. Moes, J. G. van Hasselt, J. J. Swen, and H.-J. Guchelaar. A review of mathematical models for tumor dynamics and treatment resistance evolution of solid tumors. *CPT: pharmacometrics & systems pharmacology*, 8(10):720–737, 2019.

[95] D. Yoshida, K. Kim, M. Noha, and A. Teramoto. Hypoxia inducible factor 1-α regulates of platelet derived growth factor-b in human glioblastoma cells. *Journal of neuro-oncology*, 76:13–21, 2006.

[96] H. Youssefpour, X. Li, A. Lander, and J. Lowengrub. Multispecies model of cell lineages and feedback control in solid tumors. *Journal of theoretical biology*, 304:39–59, 2012.

[97] T. Zhan, N. Rindtorff, and M. Boutros. Wnt signaling in cancer. *Oncogene*, 36(11):1461–1473, 2017.

[98] J. X. Zhou, A. O. Pisco, H. Qian, and S. Huang. Nonequilibrium population dynamics of phenotype conversion of cancer cells. *PloS one*, 9(12):e110714, 2014.